1 Motivation

As it was already pointed out in Chapter FIXME Supersymmetry is able to offer solutions to unexplained phenomena in astrophysics and can solve the shortcomings of the Standard Model of particle physics. Unfortunately, due to the unknown mechanism of supersymmetry breaking, the most general parametrization of Supersymmetry introduces over 100 new dimensions which opens up an incredibly huge phenomenalogically rich space, leading to very different possible signature at particle colliders. During the Phase I run at the LHC in 2012, a variety of different seaches, optimized on the hunt for supersymmetry were conducted. At the CMS and at the ATLAS experiments, taking data from proton-ptoton collisions, a strong focus was put on the search for hints of SUSY in the strong production sector (e.g. [1–3]). This led already to a wide exclusion in SUSY space, which nevertheless still offers some very interesting non-excluded parameter regions. The search for SUSY in more "exotic" regions gains therefore more and more attention. Typical SUSY scenarios which are not easily excluded by the general SUSY searches consists of so-called compressed spectra, where two or more particles are nearly degenerate in their masses. When mother and daughter particles are almost mass-degenerate, the remaining decay product in a two body decay can be very soft in p_T, making those scenarios very challenging to search for. Thus supersymmetric scenarios with compressed spectra are usually much weaker constrained. FIXME

One possible scenario in R-parity conserved Supersymmetry is where the lightest neutralino (χ_1^0) is almost mass-degenerate with the lighest chargino ($\chi_1^\pm$). Such a mass-degeneracy natuarally occurs in case of a wino-like neutralinos and charginos, as the mass gap is fully determined by higher loop correction as explained in Section FIXME. SUSY models with a wino-like lightest neutralino are especially interesting because they are able to explain the sources of the relic density. Althoung such a model is not able to make up the full relic density thermally produced for $m_{\chi_1^0} \lesssim 2.9$ TeV from the lightest neutralino [4], it can still be the dominant part when it is non-thermally produced via the decay of a long-lived particle [5]. A very good candidate for the long-lived particle is hence the wino-like chargino. A chargino can be produced via chargino pair production through a photon or a Z boson exchange. The chargino decays then via a virtual W boson to the lightest neutralino and fermion-fermion pair (e.g. a pion). This process is illustrated in the Feynman diagram shown in Fig. 1.1.

Other possible production channels are the exchange of a supersymmetric Higgs boson or via a t-channel squark exchange. The corresponding Feynman diagrams for the tree level production channels are shown in Fig. 1.2. Another possibility of chargino production is the chargino neutralino production channel. On tree level, there exist two production mechanism: the s-channel W boson exchange and the t-channel squark exchange. See Fig. 1.3 for the Feynman diagrams.

Even if a supersymmetric model with nearly mass-degenerate $\tilde\chi_1^\pm$ and $\tilde\chi_1^0$ leads to more exotic signatures at the CMS experiment, there have been already several analyses conducted in CMS which are in principle (even not all were designed to be) sensitive to these models. Among those are a search for long-lived charged particles [6], which was mainly

designed for particles which have such a long lifetime that they travel through the full detector without decaying and a search for disappearing tracks [7] which looked for rather intermediate lifetimes, where the charginos decays already inside the tracker. Within [7], a study was done, based on an interpretation exercise [8] within the phenomenological MSSM (see Section FIXME for a detailed introduction to the pMSSM), which tests the exclusion power for various analyses done at CMS. Figure 1.4 shows the number of excluded pMSSM space points at 95% C.L. and the fraction of excluded points as a function of the chargino lifetime for the following analyses: The search for long-lived charges particles [6] (red area), the search for disappearing tracks [7] (purple area), and a collection of many general SUSY searches at CMS [10] (blue area). The black line indicates the unexcluded pMSSM parameter points. The sampling of the parameter space points was done according to a prior probability density function which takes pre-LHC data and results from indirect SUSY searches into account (see [8] for further details). In the lower part of Fig. 1.4, it can be seen that the general SUSY searches are mostly sensitive to shorter chargino lifetimes ($c\tau \lesssim 10\,\mathrm{cm}$) whereas the search for disappearing tracks is sensitive on supersymmetric models with chargino lifetimes between $35\,\mathrm{cm} \lesssim c\tau \lesssim 100\,\mathrm{cm}$.

This analysis is targeting the gap between the disappearing track search (purple area) and the searches which are sensitive to instanteanously decaying charginos (blue area). The idea is to make use of the variable dE/dx which can be very discriminating for particles with high mass. The challenges of such a search and the general strategy of this analysis will be presented int the next section.
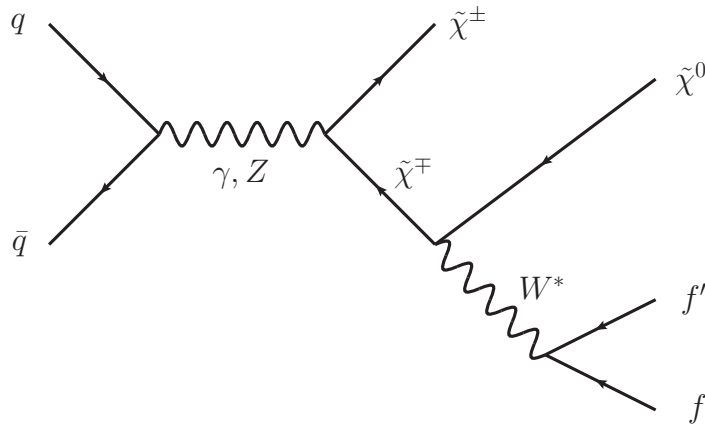

Figure 1.1: Feynman diagram showing a possible production mechanism of a chargino pair and the decay channel of a chargino.
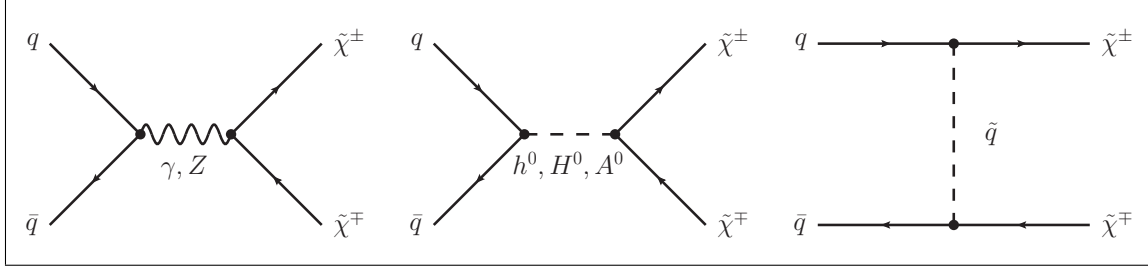
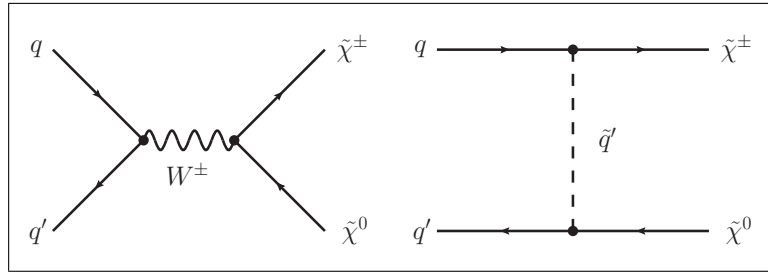Figure 1.2: Main tree level diagrams for chargino pair production.

Figure 1.3: Main tree level diagrams for chargino neutralino production.

2 General search strategy

When searching for supersymmetric models with long-lived $\tilde{\chi}_1^\pm$, the strategy is of course highly dependent on the actual lifetime of the chargino. For long lifetimes, the chargino can reach the muon chambers and can be reconstructed as a muon (even with a longer time-of-flight). For lower lifetimes, the chargino can already decay inside the detector (e.g. the tracker), hence cannot be reconstructed as a muon, but leads only to an isolated track in the tracker. The detector signatures of these two scenarios are visualised in Fig. 2.1, where in a cross-sectional view of the CMS detector simulated chargino-chargino events are shown.

As mentioned before, this analysis targets a search for supersymmetry with charginos of lifetimes between $10\,\mathrm{cm} \lesssim c\tau \lesssim 40\,\mathrm{cm}$. That means that the charginos decay rather early in the detector, even at the beginning of the tracker. The distinct challenges of such an analysis, shall be listed in the following passage.

First of all, in case R-parity (see Section **??**) is conserved, one of the decay products of the chargino, which is the lightest neutralino $\tilde{\chi}_1^0$ is stable, thus travelling through the whole detector only weakly intereacting. Therefore it is not detectable. The other chargino decay product, e.g. a pion, can be hardly reconstructed, mainly because it does not origin from the primary vertex (if the chargino reaches the detector before its decay), but secondarily because it is very low in momentum because of the mass-degeneracy between $\tilde{\chi}_1^\pm$ and $\tilde{\chi}_1^0$.
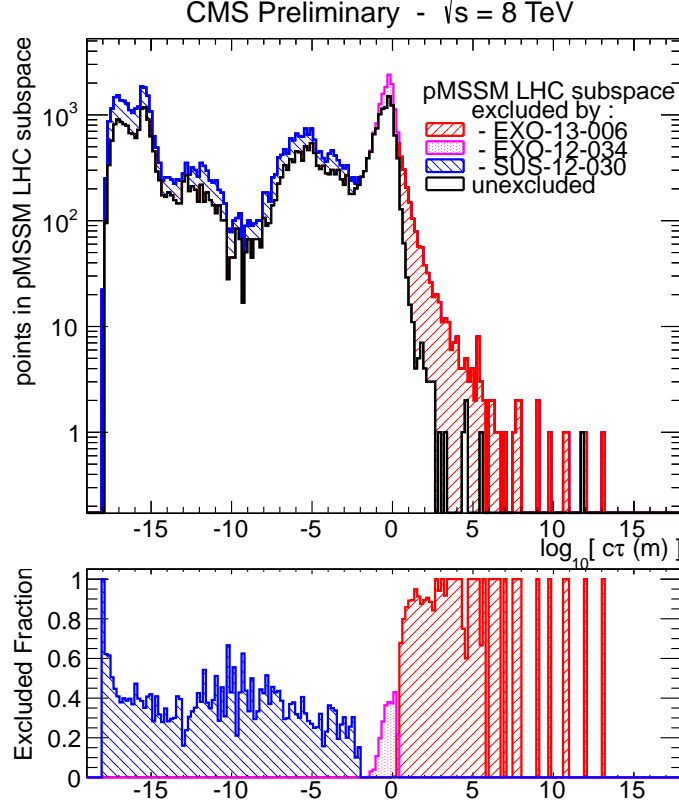
Figure 1.4: The number of excluded pMSSM space points at 95% C.L. and the fraction of excluded pMSSM space points (bottom part) vs. the chargino lifetime. Taken from: [9].

The momentum of the decay product is of course highly dependent on the actual mass gap between the neutralino and the chargino. The typical momentum of a pion originating from a chargino to neutralino decay is in the $\tilde{\chi}_1^\pm$ rest frame of the order

$$p_\pi \sim \sqrt{m_{\chi_1^\pm} - m_{\chi_1^0} - m_\pi}.$$

A p_{T} distribution of the pion for a simulation with $\sqrt{s} = 8$ TeV can be found in Fig. 2.3 for a mass gap between $\tilde{\chi}_1^\pm$ and $\tilde{\chi}_1^0$ of $\Delta m = 150$ MeV. The p_{T} distribution peaks at ~ 100 MeV and ends at $p_{\mathrm{T}} \sim 400$ MeV. When the transverse momentum of a particle is very low, the particle trajectory is much more bended compared to a particle with higher p_{T} (see Fig. 2.3 for illustration), thus making the detection of such a particle very challinging. Because of the stronger bending, the track reconstruction efficiency decreases for particles with a transverse momentum below 1 GeV rapidly, ending at around 40% for isolated pions with a p_{T} of 100 MeV (see [11]).

Taking the hard or even impossible detection of the decay products of the chargino, this lead to the fact, that besides the (short) track of the chargino, nothing can be seen in the detector. Unfortunately, there is no dedicated track trigger at CMS, which makes a specific detection of those events with the help of the chargino track impossible. To
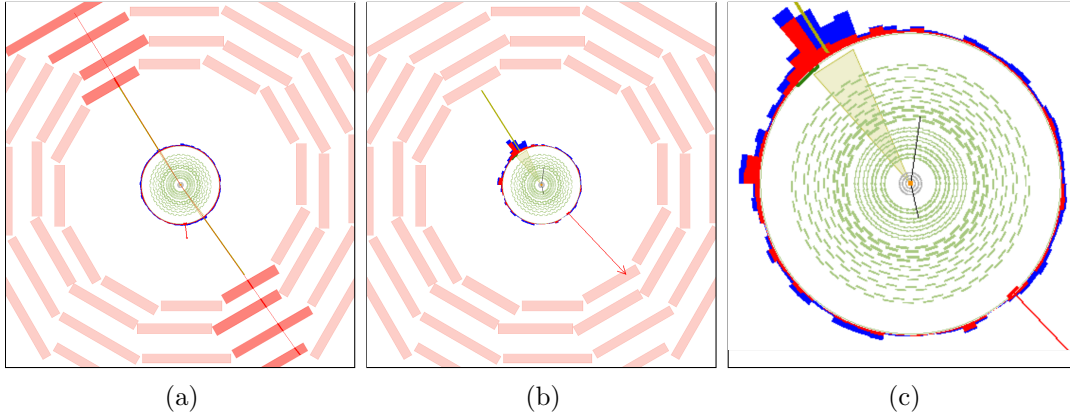
(a) (b) (c)

Figure 2.1: Visualisation of possible signatures of a chargino pair produced with a lifetime of $c\tau = 10\,\mathrm{m}$ (a) and a lifetime of $c\tau = 0.5\,\mathrm{m}$ (b and c). In the left picture, both charginos are reconstructed as muons, which can be seen in the energy deposition in the muon chambers (red boxes). In the middle picture both charginos are only visible as tracks in the tracker (black lines), where both trajectories end inside the silicon strip tracker, showing the decay point of the corresponding chargino. The right picture is a zoom of the picture in the middle. Here only the cross-section of the tracker (green wavy lines) is displayed. The red arrow shows the missing transverse energy in the event. The red (blue) towers correspond to the energy deposition in the ECAL (HCAL).

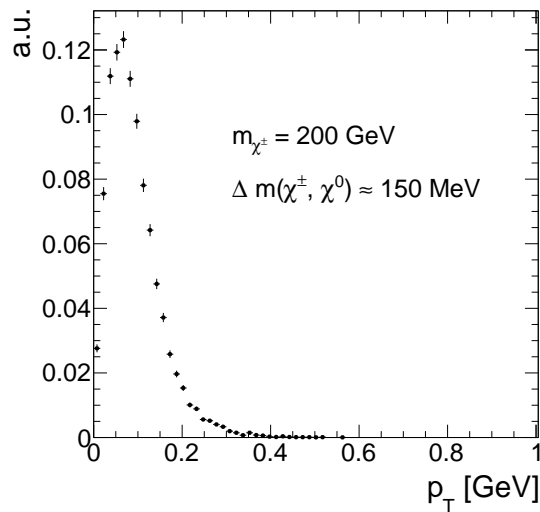be able to search for these models, one therefore needs to take advantage of higher order

Figure 2.2: Transverse momentum distribution of pions coming from chargino decay into a neutralino with a mass gap of $150\,\mathrm{MeV}$.

contributions to the feynman diagrams shown in the previous sections (Figs. 1.2, 1.3), resulting in initial state radiation (ISR). When the initial quarks radiate a high p_T gluon, the resulting jet can be detected and can offer a possibility to search for isolated tracks in the tracker. The non-detection of the chargino's decay products plus a high p_T ISR jet lead additionally to missing transverse energy (MET) in the event. Exploiding these two circumstances, it is possible to detect chargino-pair or chargino-neutralino events with the help of Jet+MET triggers.

To select possible charginos in an event, additional requirements for isolated, high p_T tracks are needed. Those tracks can be eventually disappearing, which means that the track does not cross the full pixel and strip detector. This can happen, when the chargino decays inside the tracker. For very low lifetimes, the tracks can be very short and can have only a few hits in the detector. To define a helical path five parameters are needed, therefore a minimum of three hits are required to be able to reconstruct a particle's trajectory (see [11]).

Furthermore, the massiveness of the charginos shall be exploited in this analysis, on the one hand by selecting only high p_T tracks, but on the other hand by requiering a high energy deposition per path length (dE/dx). The energy deposition depends quadratically on the particle's mass for low velocities ($0.2 < \beta\gamma < 0.9$).

$$\langle \frac{dE}{dx} \rangle = K\frac{m^2}{p^2} + C$$

thus constitute a very nice discriminating variable for massive particles against SM particles.

A specific challenge for this analysis is hence the combination of searching for short tracks and utilising the measurement of the energy deposition of the chargino. For a short track, eventually only passing the first couple layers of the whole tracker system, the pixel tracker becomes obviously very important. This means that a good energy measurement in the pixel system is of great importance to this analysis. However, no other CMS analysis used the energy information of the pixel tracker so far. That means, that a thoroughly
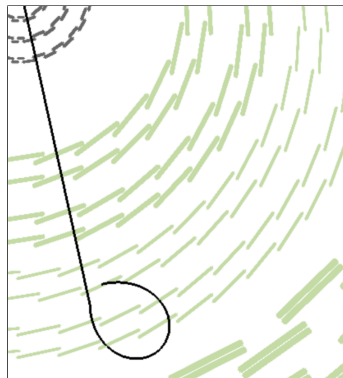

Figure 2.3: Cross-sectional view of the tracker (different tracker layers are illustrated with green lines) and a simulated chargino track (black line) decays to a pion (bended black line).

study of the quality of the pixel energy calibration needs to be undertaken, and in case the energy calibration is not suffiencient, a further energy calibration needs to be carried out.

2.1 Comparison to existing searches

As already mentioned before, there are several analyses at CMS at $\sqrt{s} = 8$ TeV with $20\,\text{fb}^{-1}$ data, which are sensitive to intermediate lifetime charginos. Most notably, the search for long lived-charged particles [6] and the search for disappering tracks [7]. An improvement in sensitivity to shorter lifetimes compared to these analysis shall be achieved in a twofold way: First, the selection in this analysis shall also include very short tracks. And secondly, also the inclusion of the variable dE/dx as discriminating variable shall increase the search sensitivity compared to [7].

In [6], for every track a minimum number of eight hits, whereas in [7] a minimum of seven hits were required. This can be very unefficient for shorter lifetimes, where most of the charginos decay already shortly after the pixel tracker. In Fig. 2.4, the normalized distribution of the number of measurements (N_{hits}) is shown. It can be seen, that for lower lifetimes, N_{hits} is peaking at the minimal possible value which is needed for track reconstruction of $N_{\text{hits}} = 3$. For higher lifetimes ($c\tau = 50\,\text{cm}$) the distribution shifts to higher values with a second peak at $N_{\text{hits}} \sim 17$. However, a notably fraction of $\sim 40\%$ of tracks has still a number of measurements below $N_{\text{hits}} < 8$.

Additionally, the search for disappearing tracks (which targets models with charginos decaying inside the tracker) did not make use of the high energy deposition of heavy particles. Although this variable was indeed used in the search for long-lived particles, this search was on the other hand not especially designed for intermediate lifetimes (e.g. no muon veto on the selected tracks was required), thus it shows less sensitivity compared to the disappearing track search in the lifetime region between $35\,\text{cm} \lesssim c\tau \lesssim 100\,\text{cm}$ (see Fig. 1.4).

Therefore to conclude, the general search strategy of the presented analysis is to unite the strategies of [6] and [7] and to lower the strong selection on the number of hits in these analyses to get an optimized selection for lifetimes around $10\,\text{cm} \lesssim c\tau \lesssim 40\,\text{cm}$.

3 Improved dE/dx measurement of short tracks

It was already pointed out, that the inclusion of the pixel energy measurements can increase the sensitivity when searching for short tracks. While the silicon strip detector has already been calibrated as part of the search for long-lived charged particles [6], there was never an offline calibration done for the pixel silicon tracker. To increase the discrimination power of dE/dx, such an calibration procedure was therefore conducted within this PHD thesis.
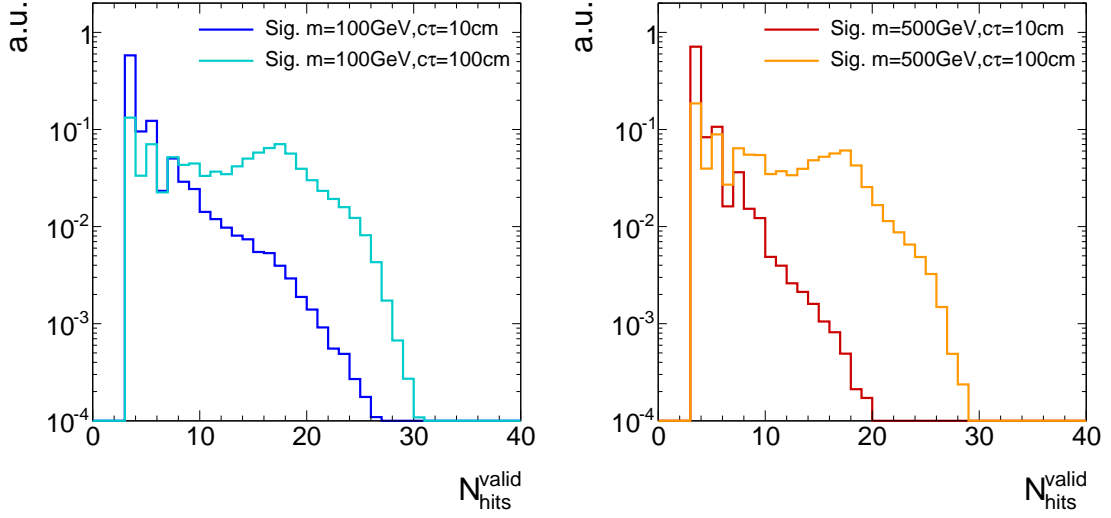
Figure 2.4: Number of measurements in the tracker system N_{hits} for two different signal lifetimes of $c\tau = 5\,\text{cm}$ and $c\tau = 50\,\text{cm}$ and two different masses: $100\,\text{GeV}$ (left) and $500\,\text{GeV}$ (right). The lower lifetime is much more rapidly falling and peaking at the lowest number of possible measurements of three. For a lifetime of $c\tau = 50\,\text{cm}$, a second peak at ~ 17 hits appears corresponding to the number of measurements when crossing all pixel barrel (3) and strip inner and outer barrel (6 from stereo and 8 from normal) layers. More information on the generation of the simulated signal samples can be found in Section 4.2

.

3.1 Ionisation loss of charged particles

The mean energy loss per path length of particles travelling through a layer of material can be described with the Bethe formula [12]:

$$\left\langle \frac{dE}{dx} \right\rangle = kz^2 \frac{Z}{A} \frac{1}{\beta^2} \left[\frac{1}{2} \ln \frac{2m_e c^2 \beta^2 \gamma^2 T_{\max}}{I^2} - \beta^2 - \frac{\delta(\beta\gamma)}{2} \right].$$

It is valid, where the main energy loss originates from ionization effects, i.e. in a region between $0.1 \lesssim \beta\gamma \lesssim 1000$. It is a function of the atomic number (Z) and the atomic mass of the absorber (A). The mean excitation energy (I) for silicon is $173\,\text{eV}$ [13]. $T_{\max}$ stands for the maximum energy transfer in a single collision. The relevant particle's properties are the velocity (β), the lorentz factor (γ) and the charge (z) of the incident particle. The density correction $\delta(\beta\gamma)$ reduces the mean energy loss at high energies because of polarization effects of the material.

Even if widely used, the mean energy loss is a quantity which is "ill-defined experimentally and is not useful for describing energy loss by single particles" [14]. The problem is caused by the underlying probability distribution of one single dE/dx measurement (this will be named by $\Delta E/\Delta x$ throughout the following sections), which can be parametrized
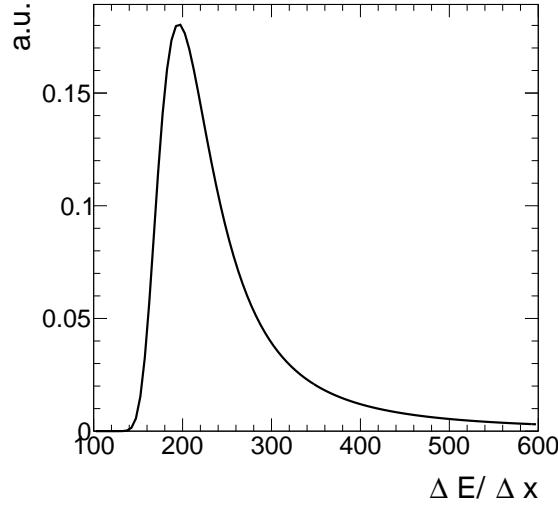
Figure 3.1: Illustration of the shape of a Landau distribution. Parameters were arbitrarily chosen for this figure.

by a Landau distribution [15]

$$p(x) = \frac{1}{\pi} \int_0^\infty e^{-t \log t - xt} \sin(\pi t) \, dt.$$

The Landau distribution is a highly asymmetric distribution with a long tail towards the right end (see Fig. 3.1). Theoretically it extends to infinite energies, however in nature the maximal deposited energy is of course limited by the particle's full energy. The mean and the variance of a landau distribution are not defined. Because of its high assymetry, measurements of $\langle dE/dx \rangle$ with only a few single measurements are easily biased torwards high values, making the mean energy loss described by the Bethe formula to a problematic and unstable concept.

A much better observable is the most probably value (MPV): the maximum of the Landau distribution. The MPV is much more stable compared to the mean and is not as easily biased towards higher dE/dx values. The most probable energy loss of a charged particle is defined by the Landau-Vavilov-Bichsel equation [16]:

$$\Delta_p = \xi \left[\ln \frac{2mc^2 \beta^2 \gamma^2}{I} + \ln \frac{\xi}{I} + j - \beta^2 - \delta(\beta\gamma) \right], \qquad (3.1)$$

with $\xi = (K/Z)\langle Z/A \rangle (x/\beta^2)$. The thickness of the absorber x appears explicitly in the Landau-Vavilov-Bichsel equation making the most probable energy loss per path length Δ_p/dx logarithmically dependent on x. A comparison between the Bethe mean energy loss $\langle dE/dx \rangle$ and the most probable energy loss Δ_p/dx is shown in Fig. 3.2. However, when measureing tracks with around ~15 hits, it is obviously not too simple to extract the most probable value. Large fluctuations can still lead to biases towards higher value of the most probable dE/dx.

There are several "estimators", which try to suppress as much as possible a bias towards
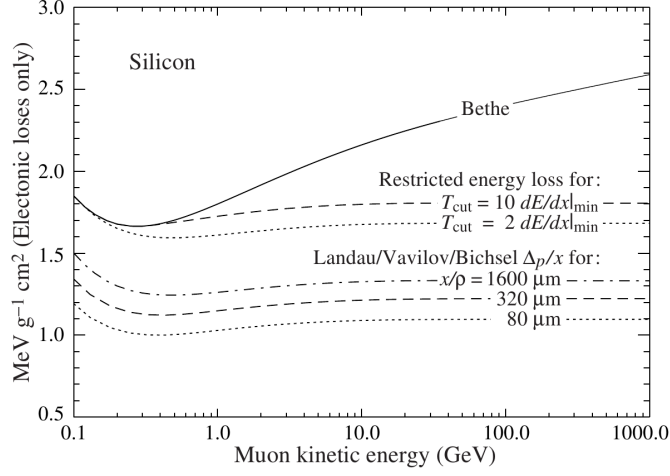
Figure 3.2: Comparison between the Bethe mean energy loss with and without restricted energy loss and the most probable energy loss described by the Landau-Vavilov-Bichsel function for different sizes of thickness. Taken from [14].

the high end, without introducing a bias to lower values. One of the estimator, also used in the next chapter, is the harmonic-2 estimator

$$I_{h2} = \left(\frac{1}{N} \sum_{i=1}^{N} (\Delta E / \Delta x)_i^2 \right)^{-1/2}, \tag{3.2}$$

where $\Delta E / \Delta x$ correspond to one measurement in one tracker module. The harmonic mean of all N measurements with the power of 2 is then the estimated most probable dE/dx.

SM particles as pions and muons are minimal ionising in silicon for $\beta\gamma \sim 4$ (see Fig. 3.3). For higher momenta the deposited energies increase again reaching a plateau at around $\beta\gamma \sim 100$. However, new heavy charged particles would mainly be unrelativistic because of their high mass and would therefore deposit much higher energies in the detector. This makes dE/dx a very well discriminating variable. Thus, the energy loss per path length can be used to discriminate between SM particles and new heavy charged particles, which are usually unrelativistic because of their high mass.

3.2 Energy calibration of the silicon pixel tracker

The CMS tracker system does not only allow for the precise measurement of particle's tracks and primary and secondary vertices but also the measurement of a particle's energy loss within the tracker material. This is done by the detection of the number of electrons produced by the ionisation of the particle during its passage through the silicon tracker. A detailed introduction about the CMS tracker system and the energy measurement can be found in Section **??**.

During Run I in 2012, the pixel silicon detector was continously subjected to an energy
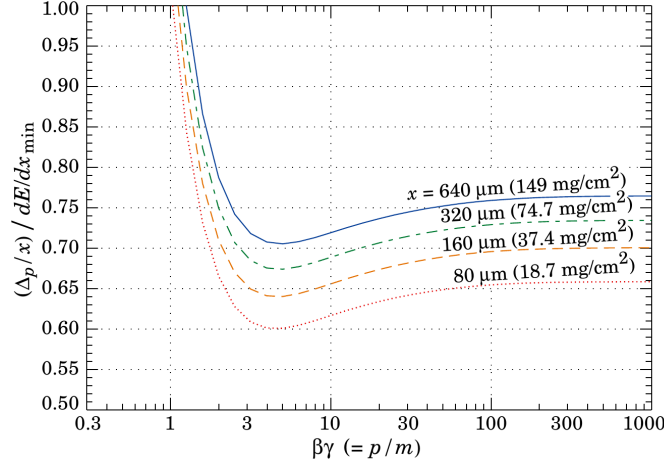
Figure 3.3: Most probable energy loss in silicon, scaled to the mean loss of a minimal ionizing particle (388 eV/μm). Taken from [14].

calibration, a so-called gain calibration. Every pixel was calibrated to the same response, such that the whole pixel tracker should have been well inter-calibrated. Unfortunately, due to various reasons, such as the imperfect constancy of the reference signal, or radiation and temperature induced changes, the energy calibration could not ensure a fully calibrated pixel tracker. This imperfection of the gain calibration can be seen in Fig. 3.4, where the sum of the harmonic-2 estimator for all tracks $\sum\limits_{\text{all trks}} I_{\text{h2}}$ over the full data-taking period in 2012 is shown. Four different steps can be spotted. The first and the third steps correspond to changes in the settings of the tracker due to irradiation. The second and fourth step
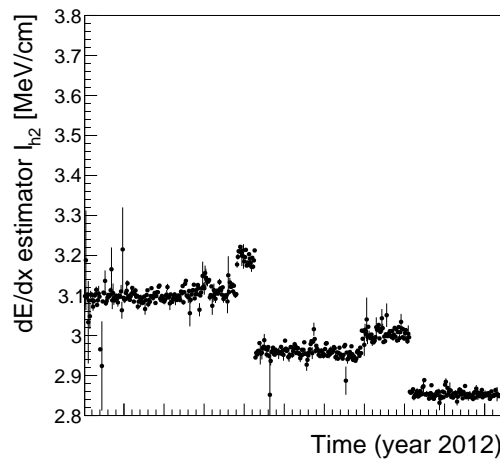

Figure 3.4: Sum of all track's dE/dx (harmonic-2 estimator) over the full year 2012. Only pixel hits are taken into account. Every data point corresponds to one run.

show the moment where an online gain calibration was again applied. Unfortunately, although a gain calibration was carried out (even with some delay), it could not bring the average dE/dx to the same level before the changes in the settings occured. The size of the difference in the dE/dx measurement over time being around 15% is too large to use dE/dx without a further calibration.

In the following sections the method of the gain calibration (splitted into an section about the inter-calibration of gain and the absolute calibration of gain) of the pixel silicon tracker is explained. Detailed technical information about the pixel tracker can be found in Section **??**.

Inter-calibration of gain

The main goal of the gain calibration is to get a uniform response in the ionization energy loss dE/dx over the full data taking period in 2012. To ensure also a uniform response of all modules within one time step, also an inter-calibration on module level was carried out. The inter-calibration can in principle be done on various stages: the highest granularity would be a calibration on pixel level, followed by a calibration on ROC-level and then on module-level. Lower granularities in descending order are rings (modules with same z-position) and finally layers (3 layers in the barrel and 4 disks in the endcap). It was checked that all pixels and all ROCs (on one module) are well inter-calibrated, such that the inter-calibration was finally done module-wise. The applied method for the gain calibration of the pixel tracker follows closely the method in [17].

The gain calibration of the pixel silicon tracker has been carried out with the help of minimal ionising particles (MIPs). MIPs in this context are not defined as particles depositing a minimum amount of energy, but more generally a small amount of energy. This denotes all particles located at the plateau of the dE/dx distribution vs. momentum (see Fig. 3.3). It ensures that all particles deposit a rather similar amount of energy such that the variation due to different momenta is suppressed. The small ionisation for particles was ensured with a momentum selection of p > 2 GeV. Additionally, only tracks with at least eight hits and a $\chi^2/n.d.o.f. < 3$ to ensure a good reconstruction were used. For the calibration a sample containing around 50 million "minimum bias" events is used which is specifically recorded for tracker calibration purposes. "Minimum bias" means that neither an online nor offline selection was applied.

For every module in the pixel tracker (there are 1440 modules in total), a distribution of the energy loss per path length $\Delta E/\Delta x$ is built. Figure 3.5 shows an example distribution for one module. The underlying Landau distribution can be nicely seen. To extract the MPV for every module a fit to the core distribution is performed. The fit is done with a Landau convoluted with a Gaussian function to be closer to the experimentally observed energy spectrum. This also increases the fit performance and the stability of the fit. The measurement of $\Delta E/\Delta x$ is done in ADC counts per mm. ADC counts are a measure for the deposited charge after digitization. It consists out of a unsigned 16-bit integer (ranging from 0 to 65 535). The path length Δx is calculated with

$$\Delta x = d_{\mathrm{module}_i} \cdot \cos(\phi_{\mathrm{track}}),$$

where d_{module_i} is the thickness of module i and ϕ_{track} is the relative angle of the particle's trajectory to the axis normal of the module. With the measured MPV extracted from the
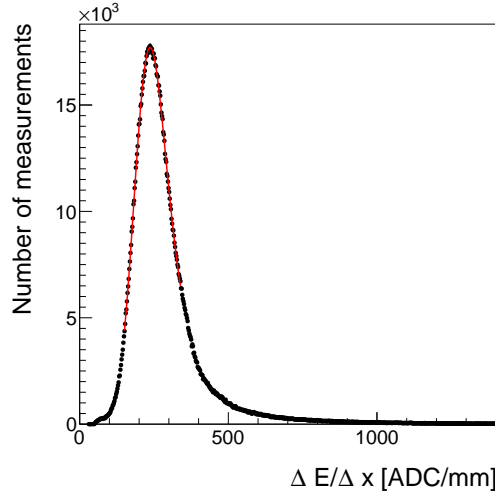
Figure 3.5: An example of the $\Delta E/\Delta x$ distribution measured in ADC count per mm for one module of the CMS pixel tracker. A Landau convoluted with a Gaussian is fitted to the core of the distribution in an iterative procedure.

fit, an inter-calibration factor is calculated for every module

$$c_{\text{inter}} = \frac{\text{MPV}\,[\text{ADC/mm}]}{\text{MPV}_{\text{target}}\,[\text{ADC/mm}]} = \frac{\text{MPV}\,[\text{ADC/mm}]}{300 \cdot 265\,\text{ADC/mm}}.$$

The factor $300 \cdot 265\,\text{ADC/mm}$ is in principal an abitrary number. However, it was choosen such that it corresponds approximately to the most probably energy deposition of a MIP. The calibration factor can then be used to scale every single measurement in a module to a calibrated $\Delta E/\Delta x$ measurement

$$\frac{\Delta E}{\Delta x}_{\text{calibrated}} = \frac{\frac{\Delta E}{\Delta x}_{\text{uncalibrated}}}{c_{\text{inter}}}$$

The determination of the calibration factor needs to be done for every of the five time steps, shown in Fig. 3.4 independently, in order to get rid of the time dependency. The result of the inter-calibration can be seen in Fig. 3.6. The variation over time was indeed eridicated, resulting in a maximal time variation of less than $\sim 1\%$.

Additionaly, the same procedure is carried out for a corresponding simulated data sample to ensure also the inter-calibration of the pixel modules on all simulated samples.

Absolute calibration of gain

As a final step, the targeted MPV being $\text{MPV}_{\text{target}} = 300 \cdot 265\,\text{ADC/mm}$ needs to be translated to a meaningful physical quantity given in phsical units (e.g. MeV/cm). That means, that the charge measurement in ADC counts needs to be converted to the real energy release of a particle. The relation between ΔE in ADC counts and the energy loss
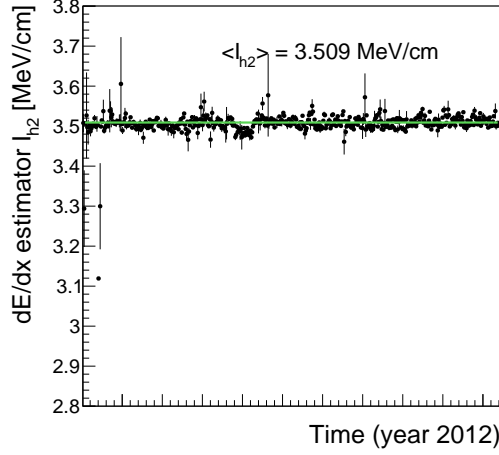
Figure 3.6: Sum of all track's dE/dx (harmonic-2 estimator) over the full year 2012 after applying the calibration factors, resulting in an average dE/dx of 3.51 MeV/cm. Only pixel hits are taken into account. Every data point corresponds to one run.

in eV is given by

$$\Delta E \, [\, \mathrm{eV}] = \frac{\Delta E \, [\mathrm{ADC}]}{c_{\mathrm{inter}}} \cdot \frac{N_e}{\mathrm{ADC}} \cdot 3.61 \ \mathrm{eV},$$

where N_e/ADC is the number of electrons which correspond to one ADC count and 3.61 eV is the mean energy needed to create one electron-hole pair in silicon at -10°C. Such an absolute gain calibration can be done with the help of several methods (all explained in [17]). For the absolute calibration of the silicon pixel tracker, it can be taken advantage of the already conducted absolute calibration of the silicon strip detector. In [17], the absolute gain calibration was done with the help of the most probable energy release per path length of muons, theoretically described by the Landau-Vavilov-Bichsel formula in Eq. 3.1. To calibrate the pixel tracker to the correct energy loss per path length it is therefore sufficient to determine one calibration factor to relate the average dE/dx of all tracks in the pixel tracker as shown in Fig. 3.6 to the average measured dE/dx in the strip tracker, shown in Fig. 3.7 by

$$c_{\mathrm{absolute}} = \frac{dE/dx_{\mathrm{strip}}}{dE/dx_{\mathrm{pixel}}} = \frac{3.303}{3.509} = 0.941.$$

This factor is then applied on top of c_{inter} for all pixel modules.

Finally, also for the simulated samples an absolute calibration factor needs to be determined, where the simulated pixel tracker is calibrated to the average dE/dx of the silicon strip measured in data.
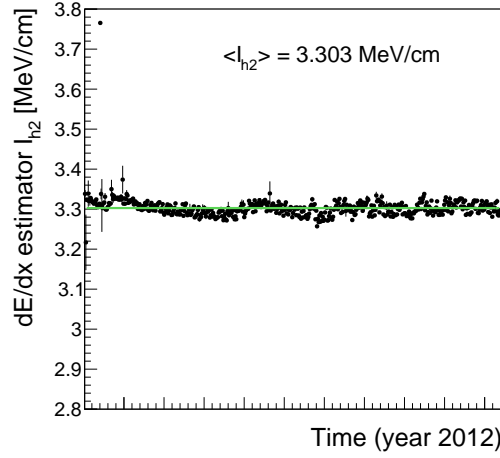
Figure 3.7: Sum of all track's dE/dx (harmonic-2 estimator) measured in the silicon strip detector over the full year 2012. The average most probable dE/dx is $I_{h2} = 3.303$ MeV/cm. Every data point corresponds to one run.

3.3 Discrimination of highly-ionising particles

As mentioned before, a difficult task when measuring the energy deposition of a particle consists in finding a robust estimator for the MPV of the underlying Landau, i.e combining eventually only a few single measurements of $\Delta E/\Delta x$ to one single dE/dx estimator. The harmonic-2 estimator I_{h2} was already introduced in Section 3.1 in Eq. 3.2. It is known as a robust estimator not easily biased by large fluctuation in $\Delta E/\Delta x$ because of the suppression by a factor of 2.

However, it was shown in [17] that a better discrimination between SM particles and possible new heavy particles can be achieved when using likelihood techniques, i.e. determining the probability that the set of all $\Delta E/\Delta x$ belonging to one track is actually compatible with the hypothetical probability distribution of a MIP.

Testing that a measured sample has been drawn from a specific distribution is know as the Smirnov-Cramér-von Mises test [18, 19], which is deduced from the integral of the squared difference of the measured distribution $P_N(x)$ to the hypothesis distribution $P(x)$

$$I_s = \int\limits_{-\infty}^{\infty} \left[P_N(x) - P(x) \right]^2 dP(x)$$

leading to a test statistics of

$$I_s = \frac{3}{N} \cdot \left(\frac{1}{12N} + \sum_{i=1}^{N} \left[P_i - \frac{2i-1}{2N} \right]^2 \right),$$

where P_i is the cumulative probability that a MIP would release a $\Delta E/\Delta x$ equal or smaller
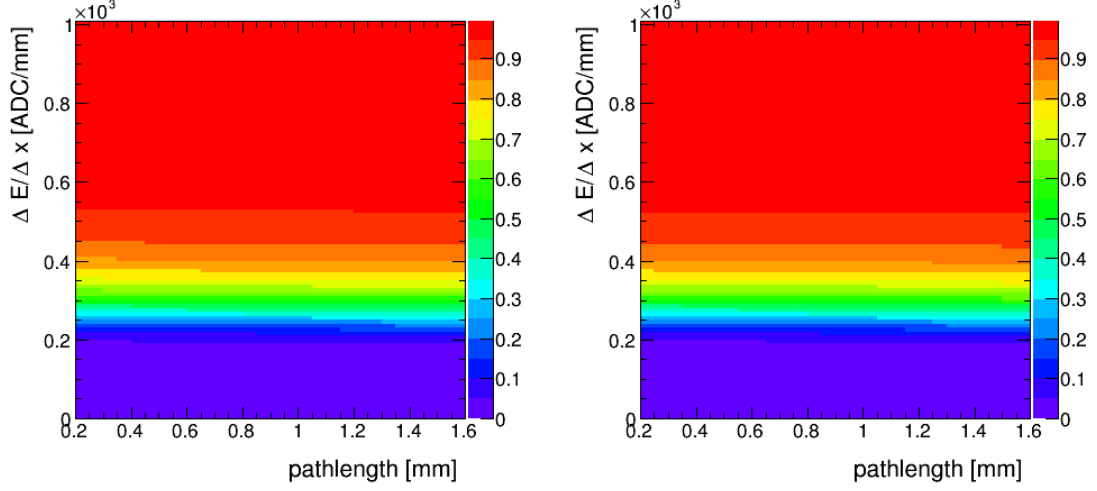
Figure 3.8: Cumulative probability for a MIP to release a $\Delta E/\Delta x$ (y-axis) vs. the path-length (x-axis) in data (left) and simulation (right) for the pixel tracker.

than the measured $\Delta E/\Delta x$ with all P_i are arranged in increasing order.

However, this test statistics is not sensitive to whether there are incompatibilities because of higher or lower variations compared to the hypothesis distribution. It is therefore not really suitable for the discrimination between MIPs and heavy new particles by dE/dx. A so-called Asymmetric Smirnov-Cramér-von Mises discriminator was developed in [17] which is only sensitive to incompatibilites to the MIP hypothesis towards higher energy depositions

$$I_{as} = \frac{3}{N} \cdot \left(\frac{1}{12N} + \sum_{i=1}^{N} \left[P_i \cdot \left(P_i - \frac{2i-1}{2N} \right)^2 \right] \right).$$

A value of I_{as} close to zero indicates good compatibility with the MIP hypothesis, whereas a value close to one indicates worse compatibility because of too large energy loss.

The underlying probability distribution of the energy release for a given path length in the pixel tracker is extracted from the same "Minimum bias" sample used for the pixel energy calibration. In total 28 different templates each for a different given path length are created. The corresponding templates for the energy release in the silicon strip detector were already built by [17]. In Fig. 3.8 the probability distribution template for the pixel tracker in data and simulation is shown. A comparison between the energy release by MIPs (I_{as}) in data and simulation for good quality tracks (high-purity as defined in [20] and minimum number of eight hits) with $p > 5\,\text{GeV}$ and $|\eta| < 2.1$ can be found in Fig. 3.9. dE/dx shows good agreement in data and simulation for $I_{as} < 0.1$. For larger values, I_{as} shows a larger decrease in simulation than in measured data. That's the reason why a data-based approach for analyses exploiting dE/dx information is needed.
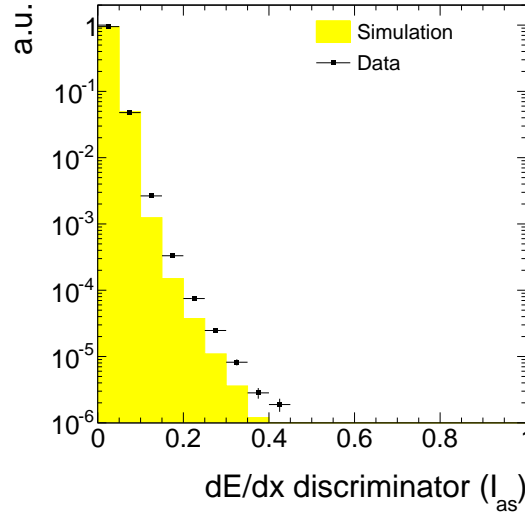
Figure 3.9: Normalized I_{as} distribution for MIPs from the minimum bias sample in data and simulation for good quality tracks with $p > 5\,\mathrm{GeV}$ and $|\eta| < 2.1$.

3.4 Discrimination improvements

The goal of including the pixel energy information is to increase the discrimination power of I_{as} between background and signal tracks, especially for shorter lifetimes. In Fig. 3.10, a comparison of the shapes of the energy release by MIPs and by signal tracks in simulation is shown (details about the simulated samples can be found in the next section Section 4.2). It can be seen, that the I_{as} distributions of the all signal models show a much longer tail toward $I_{as} = 1$, whereas the background is rapidly falling. Not only the mass of the signal track influences the I_{as} distribution but also the number of hits and the velocity (β) distribution of a signal model. The influence of the velocity can be easily seen in Eq. 3.1. This in turn results in the dependency of I_{as} on the mass of the chargino. But also for models with the same mass, the velocity is higher in average for shorter lifetimes. This is caused by the fact, that for shorter lifetimes (e.g. $c\tau = 10\,\mathrm{cm}$), already a sizeable fraction of the charginos decay before reaching the tracker system. The probability of reaching the detector increases for higher velocities, which can be clearly seen at the survival probability

$$P\left(t\right) = e^{-\frac{t}{\gamma\tau}}, \tag{3.3}$$

which shows that the survival probability is increasing for increasing β. That means shorter lifetimes lead to higher average β which in turn lead to lower I_{as}.

The number of measurements in the tracker system defines the influence of single fluctuations in $\Delta E/\Delta x$ on the I_{as} discriminator. Because of the large right tail of the Landau distribution, for tracks with a low number of hits this leads to higher I_{as} due to the fluctuations in the energy release.

That means that for models with lower lifetimes of the chargino there are two different effects: first, due to the smaller number of measurements the chargino tends to higher I_{as} values, second for low lifetime, the velocity distribution of those charginos reaching
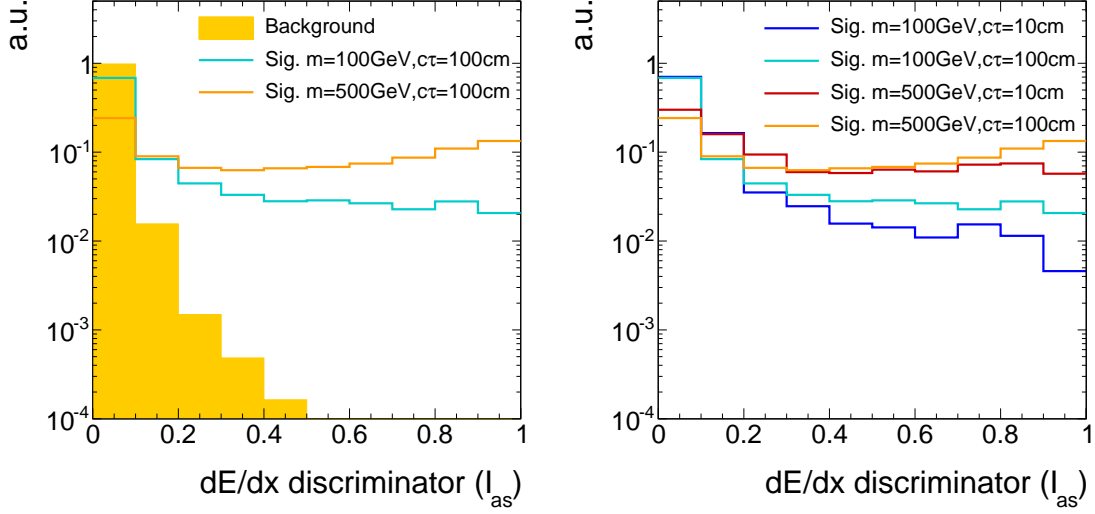
Figure 3.10: Normalized I_{as} distribution for simulated background and signal tracks (left) and for four different signal models (right) for high-purity tracks (as defined in [20]) with $p_{\mathrm{T}} > 10\,\mathrm{GeV}$ and $|\eta| < 2.1$. For the illustration of the background tracks' spectrum simulated $t\bar{t}$+jets events are used (more information about this sample is given in Section 4).

the detector is in average higher, which in turn leads to lower I_{as} values. Both effects can be seen in Fig. 3.10 (right). The large tail for longer lifetimes is caused by the lower velocities, but the small surplus between 0.1 and 0.2 is caused by the smaller number of measurments for lower lifetimes.

Finally, the impact of the additional $\Delta E/\Delta x$ information from the pixel tracker on the selection efficiency of signal and background tracks shall be quantified. Figure 3.11 shows the signal selection efficiency against the background selection efficiency for different selection cuts in I_{as}, once including the pixel information and once without it. A previous selection of good quality tracks and $p_{\mathrm{T}} > 10\,\mathrm{GeV}$ is applied. The background selection efficiency is estimated with simulated W+jets events but was additionally checked on simulated $t\bar{t}$+jets and QCD-multijet events (further information about the simulated samples can be found in the next section). No significant difference between these processes in the background selection efficiency was observed.

The signal selection efficiency and the background supression depend on the mass and the lifetime of the charginos. The discrimination power of I_{as} is as expected much better for higher masses. In addition, the impact of the inclusion of the pixel energy information is already for looser selections in I_{as} visible in the higher mass case. However, the addtional energy information shows similar impact for very strong selections for all lifetimes and masses.

For high chargino masses and small signal selection efficiencies, the background supression can be improved up to a factor of 20. For looser selections leading to higher signal efficienciey of 40%, the gain in the supression reduces to a factor of 10.
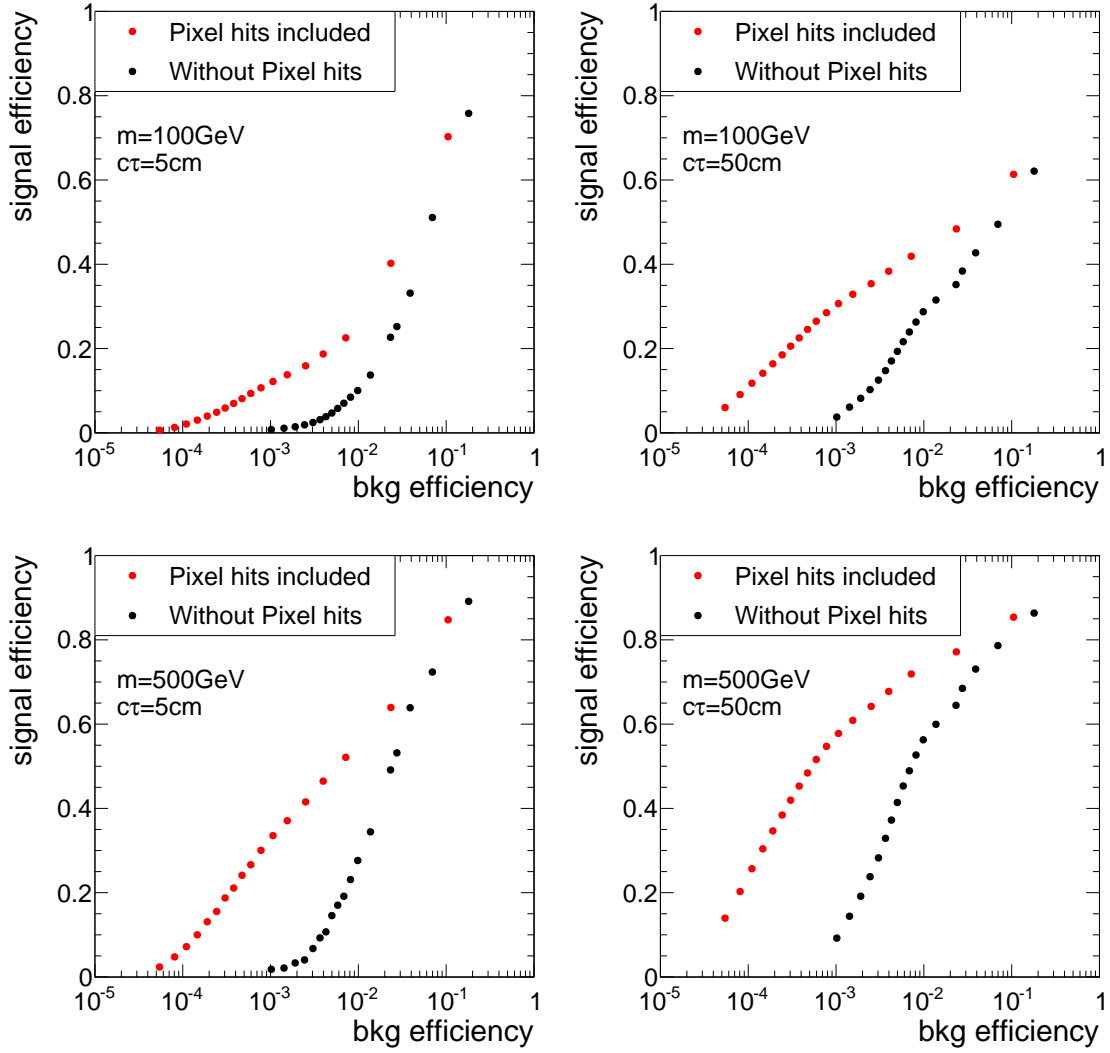
Figure 3.11: Signal selection efficiency vs. background selection efficiency when scanning through different selections in I_{as} for four different signal models.

4 Simulated samples

For the investigation of the various backgrounds, the analysis relies also on simulated samples. An extensive introduction to the techniques and tools required for the simulation of SM and beyond SM processes can be found in Section **??**.

In the following two sections an overview is given about the SM (Section 4.1) and SUSY samples (Section 4.2) used to design the search. All samples are reweighted to match the measured distribution of primary vertices in data.

4.1 Standard Model background samples

To investigate the sources of background, various simulated SM samples are used. In order to have the possibility to make use of the dE/dx variables, a special data format of the simulated samples is required (called RECO format). Unfortunately, not all SM processes were available in this specific format. However, as this analysis needs to rely anyways on a data-based background estimation method, because of the limited quality of the dE/dx simulation, it does not constitute a serious problem. It only limits the possibility of a comparison between data and simulation going beyond shape comparisons.[1]

In Table 4.1 all available SM samples used in this analysis are listed. Due to the immense size of the samples (between 5 and 70 TB) and in order to match a reasonable storage space a reduction is done by selecting only events which contain at least one leading jet with a minimum transverse momentum of $p_T > 60$ GeV.

In addition, further simulated samples not containing the energy information are used. These are needed to study the background inclusively in the variable I_{as}. They are listed in Table 4.2.

4.2 Signal samples

For the investigation of a possible signal, events containing either chargino pair production $q\bar{q} \to \tilde{\chi}_1^{\pm} \tilde{\chi}_1^{\mp}$ or chargino neutralino production $q\bar{q} \to \tilde{\chi}_1^{\pm} \tilde{\chi}_1^{0}$ are simulated. The simulation is done with the matrix-element event generator MADGRAPH [23] The parton showering and hadronisation processes are then simulated with PYTHIA [24]. A last step is needed to simulate the interactions of the generated particles with the detector material, which is done with GEANT4 [25, 26].

Furthermore, a special treatment for long-lived particles is required. In order to get the right detector simulation of the energy loss of the long-lived particles which decay after the beam pipe, the lifetime of the chargino cannot be set in the matrix-element generator

Table 4.1: Available Standard Model background samples containing $\Delta E/\Delta x$ information which are used for background estimation studies.

Process	Cross section [pb]	$\mathcal{O}_{\text{calculation}}$
W + jets	36703.2	NNLO [21]
$t\bar{t}$ + jets	245.8	NNLO [22]
$Z \to \ell\bar{\ell}$ + jets ($\ell = e, \mu, \tau$)	3531.9	NNLO [21]
QCD (50 GeV $< \hat{p}_T < 1400$ GeV)	9374794.2	LO

---

[1]E.g. the background process $Z \to \nu\bar{\nu}$ + jets sample is not available, which can possibly contribute via the fake background to the search. However, as the rate of fakes is independent of the underlying process, this background can be studied with the same quality with a W + jets sample.

Table 4.2: Standard Model background samples without $\Delta E / \Delta x$ information.

Process	Cross section [pb]	$\mathcal{O}_{\text{calculation}}$
$W + \text{jets}$	36703.2	NNLO [21]
$Z \to \ell\bar{\ell} + \text{jets} \ (\ell = e, \mu, \tau)$	3531.9	NNLO [21]

but needs to be specified within GEANT4.

To narrow down the required computing sources, the simulation is only done for a few lifetimes ($1\,\text{cm}$, $5\,\text{cm}$, $10\,\text{cm}$, $50\,\text{cm}$, $100\,\text{cm}$, $1\,000\,\text{cm}$ and $10\,000\,\text{cm}$). In order to get yet a tight scan over the lifetime space, other lifetimes are generated using lifetime reweighting. This can be done by determining a weight for every event. The weight depends on the individual proper lifetime of the chargino (in case of chargino pair production it depends on the individual lifetime of the two charginos). It is given by

$$ w = \prod_{i=1}^{n} \frac{\tau^{\text{gen}}}{\tau^{\text{target}}} \cdot \exp\left[t_i \cdot \left(\frac{1}{\tau^{\text{target}}} - \frac{1}{\tau^{\text{gen}}} \right) \right], $$

where n is the number of charginos in the event, τ^{gen} is the generated mean lifetime in the particle's rest frame and t_i is the individual proper lifetime of the chargino. The resulting mean lifetime is then given by τ^{target}. A derivation of this formula can be found in Appendix **??**. With the reweighting procedure a tight covering of the lifetime space can be achieved with lifetimes of $c\tau = a \cdot 10^n$ for $n = 0, 1, 2, 3, 4$ and $a = [1, 9]$. Figure 4.1 shows the exponential distribution of the individual proper lifetime of the charginos after the reweighting of a simulated sample with $c\tau^{\text{gen}} = 50\,\text{cm}$ to a lifetime of $c\tau^{\text{target}} = 10\,\text{cm}$. Fitting the exponential spectrum should result in the correct mean proper lifetime as parameter of the fit. It can be seen, that the reweighting procedure can reproduce the targeted lifetime of $10\,\text{cm}$.

All samples are generated for different masses of the chargino, but always almost mass-degenerate to the lightest neutralino. The mass gap between chargino and neutralino is set to $5\,\text{GeV}$. However, as this analysis does not make use of the decay products of the chargino and the lifetime is independently set within GEANT4, the mass gap does not play any role. Six different masses from $100\,\text{GeV}$ to $600\,\text{GeV}$ are simulated. This leads then to a total number of 42 signal samples. In Table 4.3 the NLO-NLL[2] cross sections at $\sqrt{s} = 8\,\text{TeV}$ for $\tilde{\chi}_1^{\pm}\tilde{\chi}_1^{\mp}$ and $\tilde{\chi}_1^{\pm}\tilde{\chi}_1^{0}$ production with wino-like charginos are listed [27, 28]. The cross section does not dependent on the lifetime of the chargino.

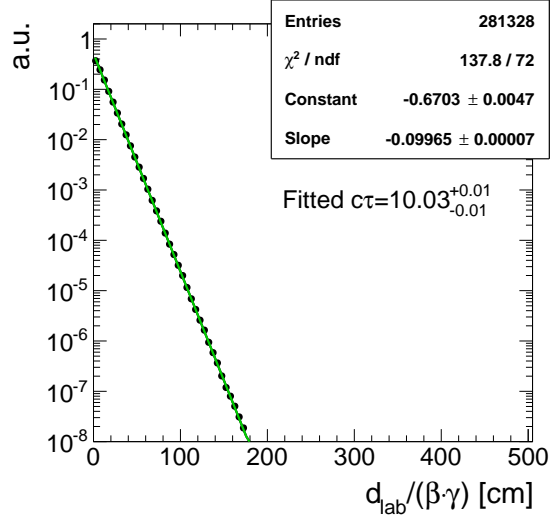[2]NLO: next-to-leading order, NLL: next-to-leading logarithmic accuracy

Figure 4.1: Normalised distribution of the proper lifetime $d_{\mathrm{lab}}/(\beta\gamma)$ of all charginos contained in a signal sample with a generated lifetime of $c\tau^{\mathrm{gen}} = 50\,\mathrm{cm}$ reweighted to a lifetime of $c\tau^{\mathrm{target}} = 10\,\mathrm{cm}$.

Table 4.3: Simulated signal mass points with corresponding cross sections for wino-like charginos.

$m_{\tilde{\chi}_1^\pm}\,[\,\mathrm{GeV}]$	$\sigma_{\tilde{\chi}_1^\pm \tilde{\chi}_1^\mp}\,[\,\mathrm{pb}]$	$\sigma_{\tilde{\chi}_1^0 \tilde{\chi}_1^\mp}\,[\,\mathrm{pb}]$
100	5.8234	11.5132
200	0.37924	0.77661
300	0.06751	0.14176
400	0.01751	0.03758
500	0.00553	0.01205
600	0.00196	0.00431

5 Event selection

5.1 Datasets and triggers

The analysis is performed on pp collision data recorded in the year 2012 at the CMS experiment for a centre-of mass energy of $\sqrt{s} = 8\,\mathrm{TeV}$. In total an integrated luminosity

of $19.7\,\mathrm{fb}^{-1}$ was recorded in 2012.

As outlined in Section 2, the detection of chargino tracks is a challenging task already on trigger level. The direct triggering of events containing chargino-like tracks is not possible because in 2012 there was no information about the tracking system on L1 level available. Furthermore, there is no intrinsic missing transverse energy in the event, when the chargino (or both charginos) decay inside the tracker. Therefore, the detection of these events shall be achieved with the help of initial state radiation. When initial state radiation occurs, it is possible to trigger on a high-p_T jet and also on $\not{E}_\mathrm{T}$ in the event.

For this purpose, several triggers are exploited. To consider the event in the analysis, at least one of them must have fired. In Table 5.1 the three triggers are listed together with the corresponding recorded integrated luminosity in the time when they were active.

Table 5.1: $\not{E}_\mathrm{T}$ and $\not{E}_\mathrm{T}$ + jet triggers used in the analysis together with the corresponding recorded integrated luminosity in the time when they were in place.

Trigger	Luminosity $[\,\mathrm{fb}^{-1}\,]$
HLTMonoCentralPFJet80_PFMETnoMu95_NHEF0p95	5.3
HLTMonoCentralPFJet80_PFMETnoMu105_NHEF0p95	14.4
HLT_MET120_HBHENoiseCleaned	19.7

The HLTMonoCentralPFJet80_PFMETnoMu95_NHEF0p95 and HLTMonoCentralPF-Jet80_PFMETnoMu105_NHEF0p95 triggers exploit both the L1 ETM40 trigger, which requires the missing energy to be larger than $40\,\mathrm{GeV}$. On HLT level, they require further at least one PF jet with $p_\mathrm{T} > 80\,\mathrm{GeV}$ and the missing transverse momentum $\not{E}_\mathrm{T}$ (not taken into account the p_T of any muon in the event) to be larger than $95\,\mathrm{GeV}$ (or $105\,\mathrm{GeV}$). Finally, the energy release by neutral hadrons must not be larger than 95% for all jets in the event. The HLTMonoCentralPFJet80_PFMETnoMu95_NHEF0p95 trigger was in place during Run A and Run B in 2012 data taking, whereas HLTMonoCentralPF-Jet80_PFMETnoMu105_NHEF0p95 was set during Run C and Run D in 2012.

The HLT_MET120_HBHENoiseCleaned trigger is based on the two L1 triggers ETM40 and ETM36 which are combined by a logical OR. On HLT level, the trigger requires that the missing energy measured in the calorimeter is larger than $120\,\mathrm{GeV}$. The HBHENoise-filter reduces background from electronic noise in the HCAL.

Table 5.2 lists the datasets in which the triggers used in the analysis are comprised. Again, because of the size of the datasets ($\sim 150\,\mathrm{TB}$ in total), a reduction of the size is achieved by selecting only events with at least one jet with a minimum p_T of $50\,\mathrm{GeV}$.

In addition, the analysis makes use of the datasets listed in Table 5.3. These datasets are used for background estimation purposes and the estimation of their associated systematic uncertainties.

Table 5.2: MET data samples used in the search with the contained integrated luminosity.

Dataset	Luminosity [fb^{-1}]
/MET/Run2012A-22Jan2013-v1/RECO	0.876
/MET/Run2012B-22Jan2013-v1/RECO	4.412
/MET/Run2012C-22Jan2013-v1/RECO	7.055
/METParked/Run2012D-22Jan2013-v1/RECO	7.354

Table 5.3: Further datasets used for background estimation.

Dataset	Luminosity [fb^{-1}]
/SingleMu/Run2012A-22Jan2013-v1/AOD	0.876
/SingleMu/Run2012B-22Jan2013-v1/AOD	4.405
/SingleMu/Run2012C-22Jan2013-v1/AOD	7.040
/SingleMu/Run2012D-22Jan2013-v1/AOD	7.369
/SingleElectron/Run2012A-22Jan2013-v1/AOD	0.876
/SingleElectron/Run2012B-22Jan2013-v1/AOD	4.412
/SingleElectron/Run2012C-22Jan2013-v1/AOD	7.050
/SingleElectron/Run2012D-22Jan2013-v1/AOD	7.368

5.2 Analysis selection

In order to suppress events originating from SM processes (such as QCD-multijet events, W + jets, etc.), a selection for signal-like tracks is applied which shall be described in the following sections. The candidate track selection follows closely the selection required in [29, 30].

Event based selection

First, to suppress cosmic events and noise from the beam halo a selection on the quality of the vertex can be applied. This selection includes requirements of the position of the vertex with respect to the beam axes and the number of degrees of freedom (which is strongly correlated to the number of tracks originating from the vertex) [31]:
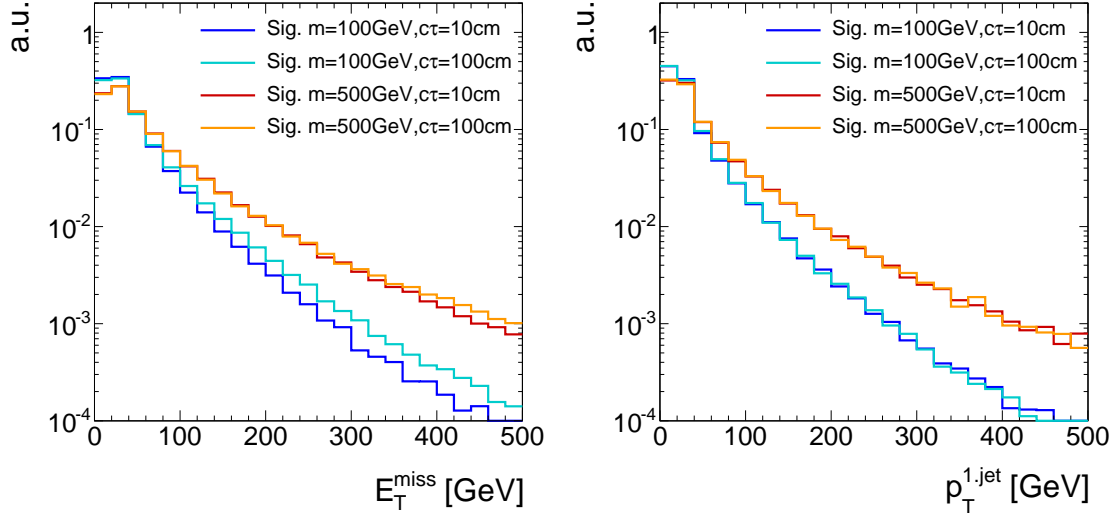
Figure 5.1: Normalised distributions of the missing transverse momentum (left) and the transverse momentum of the leading jet (right) for four different signal models.

❖ The vertex must have at least four degrees of freedom: vtx with ≥ 4 d.o.f.

❖ The position of the vertex along the beam line must be within $24\,\mathrm{cm}$ from the beam origin: $|dz| \leq 24\,\mathrm{cm}$.

❖ The position in the transverse direction must be within $2\,\mathrm{cm}$ from the beam origin: $|d0| \leq 2\,\mathrm{cm}$.

After these selection cuts are applied the remaining events are subjected to a further pre-selection.

To maximise the signal acceptance, the trigger related selection cuts are chosen as close as possible to the trigger thresholds (see Section 5.1). In Fig. 5.1, the distributions of $\not{E}_{\mathrm{T}}$ and the transverse momentum of the leading jet $p_{\mathrm{T}}^{1.\,\mathrm{jet}}$ are shown for different signal models. Only jets are taken into account with $|\eta| < 2.4$ and which fulfil several further criteria:

• Charged hadron energy fraction > 0.2

• Charged electromagnetic energy fraction < 0.5

• Neutral hadron energy fraction < 0.7

• Neutral electromagnetic energy fraction < 0.7.

These additional jet quality criteria ensure that noise from cosmic and beam halo muons and high-p_{T} photons and electrons is suppressed [32]. In can be seen in Fig. 5.1 that already for a selection of $\not{E}_{\mathrm{T}} > 100\,\mathrm{GeV}$ 80% of the signal events are rejected.

The trigger efficiency as a function of $\not{E}_T$ and $p_T^{1,\,\mathrm{jet}}$ was determined within [33] with a single-muon reference sample. The trigger paths become fully efficient for $p_T^{1,\,\mathrm{jet}} \gtrsim 110\,\mathrm{GeV}$ and $\not{E}_T \gtrsim 220\,\mathrm{GeV}$ [32].

However, as said before, this search imposes a trigger selection to maximise the signal acceptance. The trigger requirement are as follows:

❖ There is at least one jet within $|\eta| < 2.4$ with transverse momentum larger than 110 GeV which fulfils the above mentioned jet noise cleaning criteria: $p_T^{1,\,\mathrm{jet}} > 110\,\mathrm{GeV}$.

❖ The missing transverse momentum must be larger than 100 GeV: $\not{E}_T > 100\,\mathrm{GeV}$

Because of the huge cross section, QCD-multijet events are frequently produced at the LHC. Due to jet energy mismeasurements, they can also contribute to data samples recorded with MET triggers. Therefore, some special requirements to suppress events emerging from strong production processes are enforced. QCD-multijet events can be characterised by topologies were two jets are almost back-to back. Additionally, in QCD-multijet events the missing energy is usually aligned with one of the leading jets in the event. Therefore the following two requirements are sufficient to suppress QCD-multijet events efficiently:

❖ $\Delta\phi$ between any of two subleading jets (with $p_T < 20\,\mathrm{GeV}$ and $|\eta| < 4.5$) in the event must be smaller than 2.5.

❖ $\Delta\phi$ between any of the two leading jets (with $p_T < 20\,\mathrm{GeV}$ and $|\eta| < 4.5$) and the $\not{E}_T$ must be larger than 0.5.

Figure 5.2 shows the maximal $\Delta\phi$ of any of two subleading jets and the minimal $\Delta\phi$ between the $\not{E}_T$ vector and the first two subleading jets for the SM background and two different signal datasets.

Candidate track selection

After the reduction of background processes with event based variables, a track based selection is carried out. To get an optimised selection for possible chargino tracks several signal track characteristics are exploited.

First a selection of tracks of good quality is enforced:

❖ The track must be of "high purity" as defined in [20].

❖ The track is required to have no missing middle or inner hits: $N_{\mathrm{miss}}^{\mathrm{middle/inner}} = 0$

❖ The radial and longitudinal distance of the track to the primary vertex must be small: $|d0| < 0.02\,\mathrm{cm}$, $|dz| < 0.5\,\mathrm{cm}$.

In Figs **??**, 5.3 and 5.4, the power of the quality selection cuts are shown.

Furthermore, a first kinematic preselection is applied:

❖ Only tracks are considered which are within the tracker acceptance taken an isolation cone into account: $|\eta| < 2.1$.
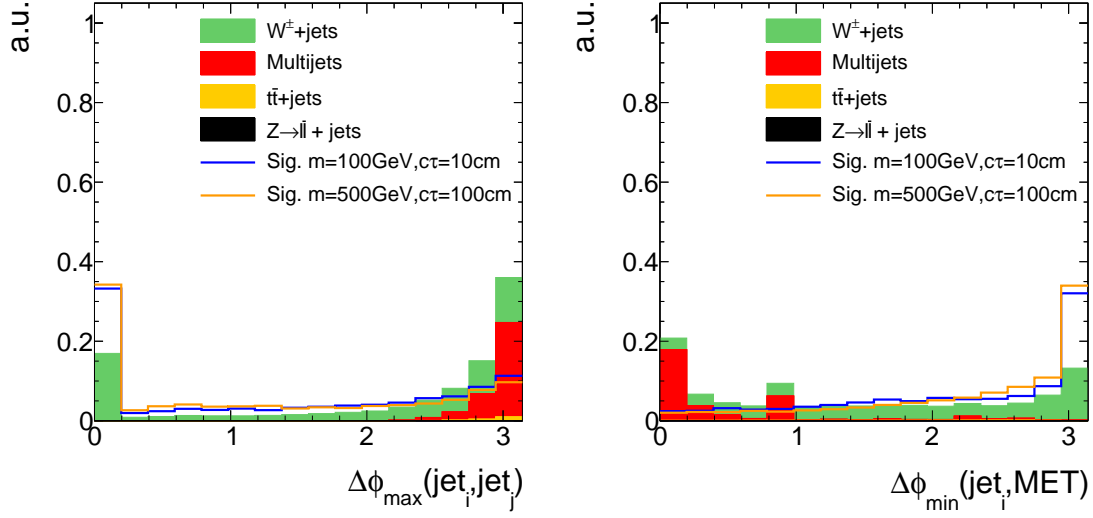
Figure 5.2: Maximal $\Delta\phi$ between any of two subleading jets (left) and the minimal $\Delta\phi$ between the $\not{E}_T$ vector and the first two jets (right) normalised to unit area after the trigger selection.
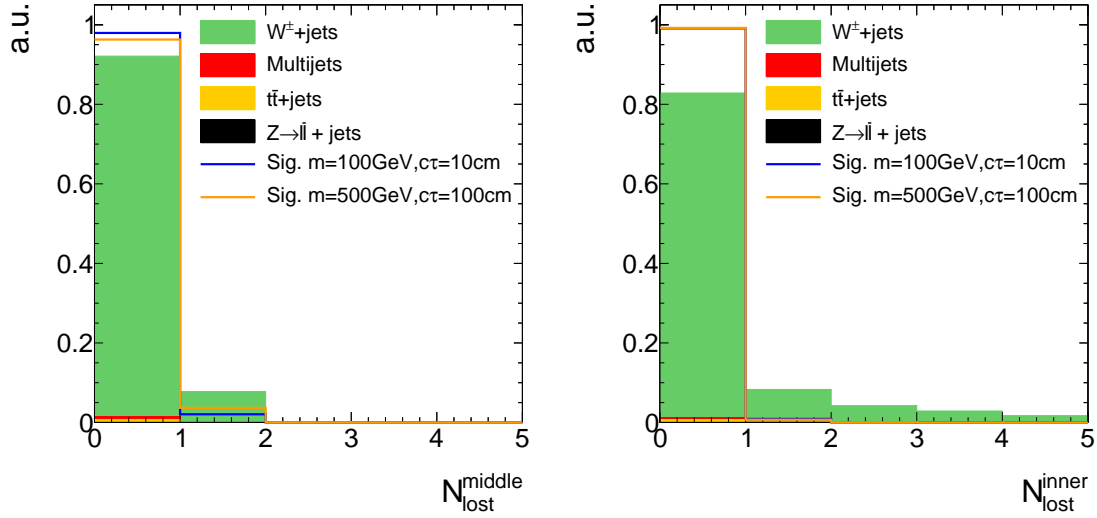

Figure 5.3: Number of missing middle (left) and inner (right) hits of background and signal tracks after trigger requirements and QCD suppression cuts.

❖ A first loose selection of tracks in the transverse momentum is applied: $p_T > 10\,\text{GeV}$.

In order to suppress background tracks emerging from SM processes, an electron, muon and tau veto is applied. That means events containing a candidate tracks close to a reconstructed electron, muon or tau are rejected. Additionally, the candidate track must not be close to a subleading jet ($p_T < 20\,\text{GeV}$ and $|\eta| < 4.5$).
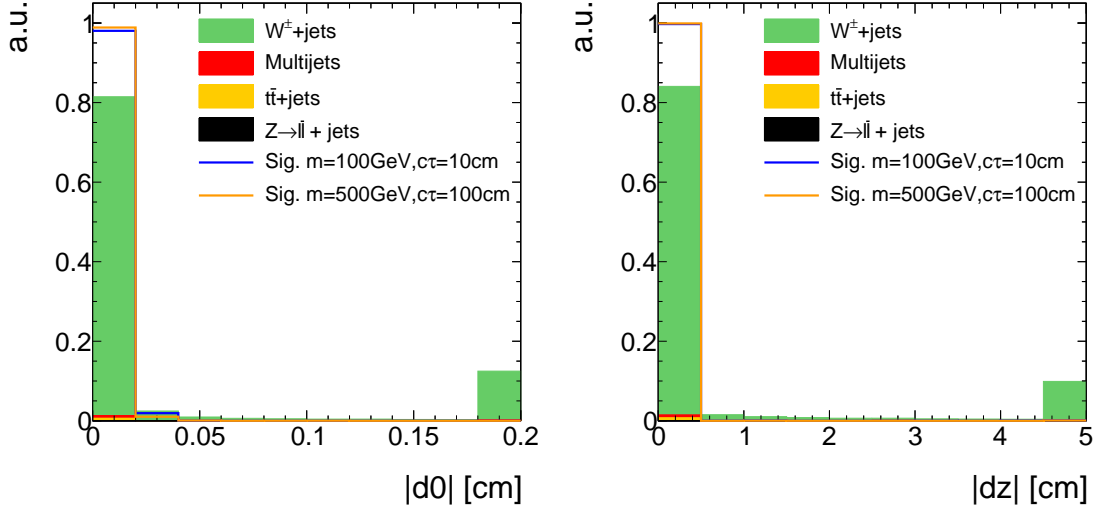
Figure 5.4: Absolute value of the radial (left) and longitudinal (right) distance between the track and the primary vertex after trigger requirements and multijet suppression cuts. Overflow entries are added to the last bin.

Unfortunately, the lepton veto selection cuts lack efficiency in some of the detector directions. For example, the reconstruction of an electron easily fails in the direction of a dead ECAL cell. This reduces the discrimination power of the electron veto. For this reason, tracks which point to a dead ECAL cell are rejected. A general list of dead and noisy ECAL cells is provided centrally at CMS. Further dead cells were identified within a study in [7] resulting in a total number of 1234 dead or noisy ECAL channels. These are illustrated in Fig. 5.5 showing a map of all ECAL channels not considered in the search.

Additionally, also tracks which point towards intermodule gaps of ECAL cells or to the ECAL barrel endcap gap at $1.42 < |\eta| < 1.65$ are rejected. A list of the ECAL intermodule gaps is given in Table 5.4.

The muon reconstruction is less efficient for muons in detector regions with bad cathode strip chambers (CSC). Thus, also tracks pointing in these regions within a distance of $\Delta R < 0.25$ are rejected.

To summarise, the candidate track must fulfil the following selection criteria:

❖ The track must not be within a cone of $\Delta R < 0.15$ to a reconstructed standalone, tracker or global muon with a transverse momentum larger than $10\,\mathrm{GeV}$.

❖ Veto all tracks within a cone of $\Delta R < 0.15$ to a reconstructed electron with a transverse momentum larger than $10\,\mathrm{GeV}$.

❖ The track must not be within a cone of $\Delta R < 0.15$ to a reconstructed tau with $p_\mathrm{T} > 20\,\mathrm{GeV}$ and $|\eta| < 2.3$.

❖ No subleading jet ($p_\mathrm{T} < 20\,\mathrm{GeV}$ and $|\eta| < 4.5$) is allowed around the track in a cone of $\Delta R < 0.5$

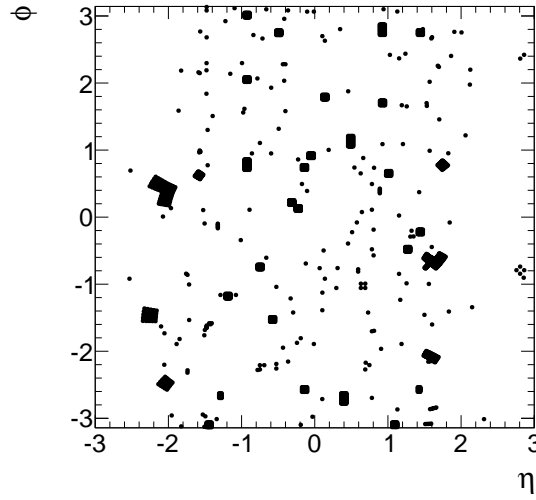❖ Veto tracks within a cone of $\Delta R < 0.05$ to a dead or noisy ECAL cell.

Figure 5.5: Visualisation of dead and noisy ECAL cells in the detector's $\phi - \eta$ plane.

Table 5.4: Intermodule ECAL gaps.

η-ranges
-1.14018 < η < -1.1439
-0.791884 < η < -0.796051
-0.44356 < η < -0.447911
0.00238527 < η < -0.00330793
0.446183 < η < 0.441949
0.793955 < η < 0.789963
1.14164 < η < 1.13812

❖ The track must not point in the direction of the ECAL intermodule gap listed in Table 5.4.

❖ The track must not be within a cone of $\Delta R < 0.25$ to a bad CSC.

❖ Veto any track pointing to the region between ECAL barrel and endcap at $1.42 < |\eta| < 1.65$

Figure **??** shows a the minimal ΔR between the candidate track and a reconstructed electron, muon or tau. As can be seen, these selection cuts can efficiently reduce the $W +$ jets background.
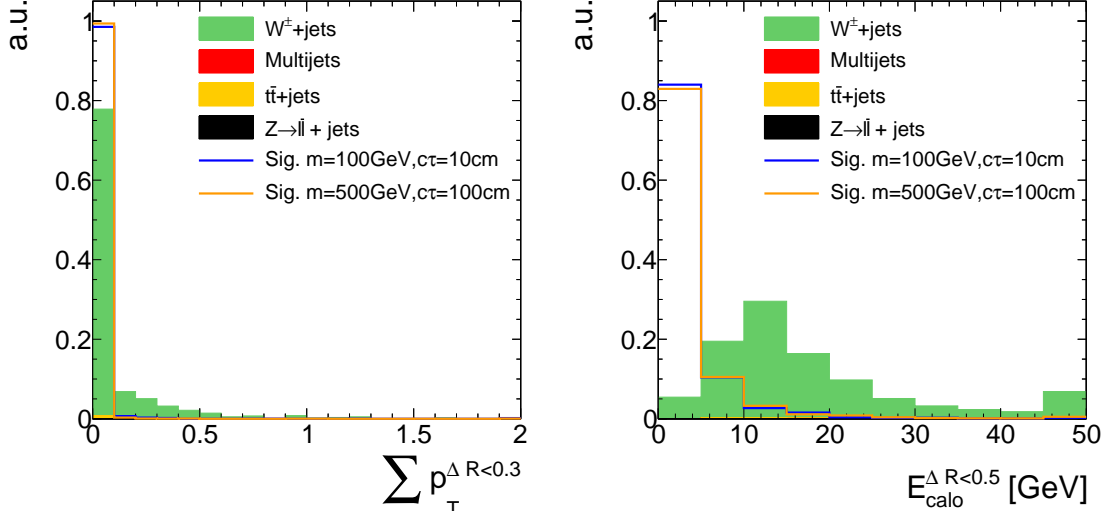
Figure 5.6: Track isolation (left) and calorimeter isolation (right) of the candidate track after the full previous selection (after all other selection cuts of the candidate track selection).

Finally, two further pronounced characteristics of chargino tracks are exploited. As the chargino is produced in a very clean environment, the isolation of the track (defined as the sum of all track's transverse momentum in a cone of $\Delta R < 0.3$ around the candidate track) can discriminate signal against background events.

Furthermore, for charginos decaying inside the tracker there is no associated energy deposition in the calorimeters in the direction of the track. This is a very pronounced characteristics of signal tracks.

The concrete selection cuts are as follows

❖ No further substantial track activity (less than 10%) is allowed in a cone of $\Delta R < 0.3$ around the candidate track: $\sum\limits_{\Delta R < 0.3} p_{\mathrm{T}}/p_{\mathrm{T}}^{\mathrm{cand}} < 0.1$

❖ Little calorimeter energy deposits (ECAL+HCAL) in a cone of $\Delta R < 0.5$ around the track: $E_{\mathrm{calo}}^{\Delta R < 0.5} < 5\,\mathrm{GeV}$.

The discrimination power of these two variables is shown in Fig. 5.6.

As emphasised before, this analysis aims to be as general as possible to search for charginos with different lifetimes. Although the search is designed with a focus on charginos which decay inside the tracker, no explicit selection cut is required in the number of missing outer hits. For charginos with very short mean lifetimes it was checked, whether a sensitivity increase can be achieved by imposing a cut on $N_{\mathrm{miss}}^{\mathrm{outer}}$. However, this is not the case and therefore a selection in $N_{\mathrm{miss}}^{\mathrm{outer}}$ is not considered.

An overview over the analysis preselection is given in Table 6.1.

Table 5.5: Summary and categorisation of the analysis selection.

Trigger		HLTMonoCentralPFJet80_PFMETnoMu95_NHEF0p95
		HLTMonoCentralPFJet80_PFMETnoMu105_NHEF0p95
		HLT_MET120_HBHENoiseCleaned
Event based selection	Trigger selection	$p_T^{1.\,\mathrm{jet}} > 100\,\mathrm{GeV}$ with $\|\eta_{1.\mathrm{jet}}\| < 2.4$, $\mathrm{CHF}_{1.\mathrm{jet}} > 0.2$, $\mathrm{CEF}_{1.\mathrm{jet}} < 0.5$, $\mathrm{NHF}_{1.\mathrm{jet}} < 0.7$, $\mathrm{NEF}_{1.\mathrm{jet}} < 0.7$ $\not{E}_T > 100\,\mathrm{GeV}$
	QCD supression	$\Delta\phi_{\max}\left(\mathrm{jet}_i, \mathrm{jet}_j\right) < 2.7$ for all jets with $p_T > 20\,\mathrm{GeV}, \|\eta\| < 4.5$ $\Delta\phi_{\max}\left(\mathrm{jet}_i, \not{E}_T\right) > 0.5$ for two leading jets
Candidate track selection	Good quality selection	≥ 1 high-purity track ≥ 1 track with $N_{\mathrm{miss}}^{\mathrm{middle/inner}} = 0$ ≥ 1 track with $\|d0\| < 0.02\,\mathrm{cm}$ ≥ 1 track with $\|dz\| < 0.5\,\mathrm{cm}$
	Kinematic selection	≥ 1 track with $\|\eta\| < 2.1$ ≥ 1 track with $p_T > 10\,\mathrm{GeV}$
	Lepton/jet veto	≥ 1 track without a muon within $\Delta R < 0.15$ ≥ 1 track without an electron within $\Delta R < 0.15$ ≥ 1 track without a tau within $\Delta R < 0.15$ ≥ 1 track without a jet within $\Delta R < 0.5$ ≥ 1 track not within $\Delta R < 0.05$ of a dead/noisy ECAL cell ≥ 1 track not within an ECAL intermodule gap ≥ 1 track not within $1.42 < \|\eta\| < 1.65$ ≥ 1 track not within $\Delta R < 0.25$ to a bad CSC
	Isolation selection	≥ 1 isolated track $\sum\limits_{\Delta R < 0.3} p_T / p_T^{\mathrm{cand}} < 0.1$ ≥ 1 track with $E_{\mathrm{calo}}^{\Delta R < 0.5} < 5\,\mathrm{GeV}$

```
figures/analysis/AnalysisSelection/chfTgarks/ahaXysestAnaNySrsggeeCutenAthaTkRtXmahlR8
```

Figure 5.7: Candidate track p_T (left) and I_{as} (right) after the full candidate track selection for signal and $W +$ jets events. Because of high event weights of the $W +$ jets sample, the $\not{E}_T$ and $p_T^{1.\,jet}$ cuts are loosen to $\not{E}_T > 0\,\text{GeV}$ and $p_T^{1.\,jet} > 70\,\text{GeV}$. As these variables are not expected to be correlated with the track characteristics it does not influences the shape of the shown distributions.

A cutflow of the simulated background datasets and for some of the signal models can be found in Appendix ??.

Given the presented candidate selection requirements, a set of two variables remain, which are highly discriminating: The transverse momentum and the energy release per path length of the candidate track. In Fig. 5.7, the distribution of the remaining two variables are shown after the application of the full candidate track selection. These variables are used to optimise the sensitivity of the search in the variable $S/(S + B)$ (S=number of signal events, B=number of background events). The optimisation process will be explained in Sec ??. However, before the optimisation can be accomplished, the characterisation end estimation of the background is needed. This topic will be discussed in the following section.

6 Characterisation and estimation of the Standard Model backgrounds

After the application of the candidate track selection explained in the previous section the background arising from Standard Model processes is dramatically reduced. However, it still happens sometimes that an electron, muon or tau fails reconstruction. The underlying mechanism and the methods to estimate the leptonic background will be in detail explained
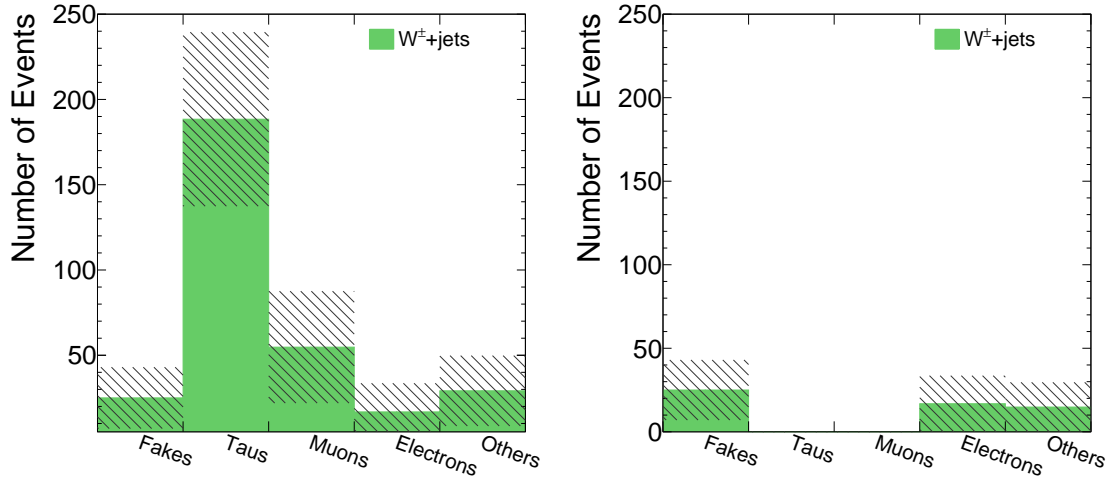
Figure 6.1: Background composition after the full candidate track selection (left) and after the full candidate track selection plus an additional selection cut of $I_{as} > 0.05$ (right). The statistical uncertainty is depicted by the hashed grey area. Given the limited size of the simulated W + jets dataset, the uncertainty of the composition is accordingly large.

in Section **??**. Furthermore, there is the possibility that a track is reconstructed out of a set of hits which do not origin from only one single particle. Such tracks are called "fake tracks". Background tracks arising from the wrong combination of hits will be explained in the following Section 6.1

The composition of the background after the candidate track selection is shown in Fig. 6.1. This composition can change significantly when imposing further selection cuts on p_T and I_{as}. This, however, will be addressed during the optimisation procedure. To get a feeling how the composition of the background is affected by further cuts on one of the main variables, the background composition is also shown with the candidate track selection plus an additional I_{as} cut of 0.05. It can be seen that the fake background is less reduced by an additional selection cut on I_{as}. This gains even more in importance when considering all sources of fake tracks. The fake background is not only present in W + jets events but essentially in all Standard Model processes.

Still, also the leptonic background can be important. Unfortunately, because of the limited size of the simulated W + jets dataset, it is not possible to study the leptonic contribution to the background with simulated events. Furthermore, when the simulation of the operativeness of every single detector module is not fully correct, the simulation could highly underestimate the leptonic background.

Therefore, a data-based approach is needed for either of the two background sources: the fake and the leptonic background.
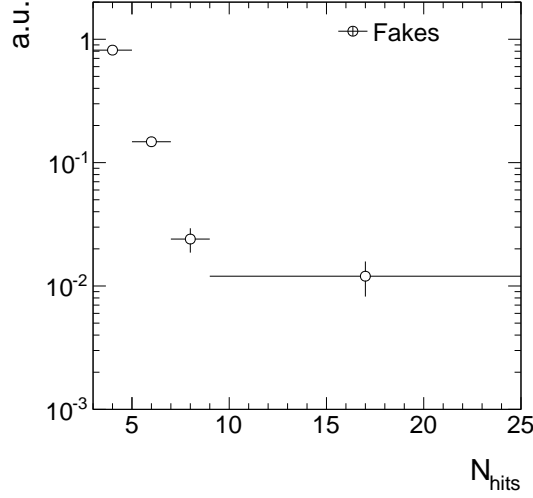
Figure 6.2: Normalised distribution of the number of hits for fake tracks.

6.1 Fake background

Fake tracks are tracks which are not reconstructed out of the trajectory of one single particle. The rate with which this wrong reconstruction occurs is of course highly restrained by the quality cuts on χ^2 and the vertex compatibility of the track reconstruction algorithm. Details on the reconstruction algorithm at CMS can be found in Section **??**. The probability of reconstructing a fake track is strongly correlated with the number of hits in the tracker system. This can be seen in Fig 6.2, where the distribution in the number of hits of fakes is depicted. There are almost no fakes with a number of hits larger than six. In simulation, fake tracks are defined as tracks which cannot be matched to a generator-level particle within a distance of $\Delta R < 0.01$.

Fakes are efficiently suppressed by the requirements of no missing middle or inner hits and the compatibility with the primary vertex. Unfortunately, wrongly reconstructed tracks which pass these criteria, do also easily pass the $E_{\mathrm{calo}}^{\Delta R < 0.5} < 5\,\mathrm{GeV}$ requirement with high efficiency.

In this analysis, the estimation of the fake background is split into two parts. First, the background is estimated inclusively in I_{as}. Secondly, to be able to optimise later in the variable I_{as}, the I_{as} distribution is taken from a fake enriched control region.

Inclusive fake background estimation

The inclusive background estimation follows closely the background estimation method done in [29, 30]. The inclusive fake background is estimated with the help of $Z \to \mu\bar{\mu}$ and $Z \to e\bar{e}$ events. Selecting clean $Z \to \ell\bar{\ell}$ events can be done with high efficiency **??** by requiring two well reconstructed muons or electrons, for which the invariant mass is around the Z-boson mass of $\sim 90\,\mathrm{GeV}$. Putting on top the candidate track selection described in Section 5.2, the selected track must a fake.

To select well reconstructed muons, the following cuts are required: The full event selection for this electron/muon control sample is given in Table **??**.

Table 6.1: Event selection cuts for the muon control sample to estimate the inclusive fake background.

Event based selection	Two global muons with $p_{\mathrm{T}} > 25\,\mathrm{GeV}$
	$\|\eta < 2.4\|$
	$\sum p_{\mathrm{T}}/p_{\mathrm{T}}(\mu) < 0.12$
	$\left.\frac{\chi^2}{ndof}\right\|_{\text{global track}} < 10$
	$\|d0\| < 0.2\,\mathrm{cm}$
	$\|dz\| < 0.5\,\mathrm{cm}$
	≥ 1 hit in the muon detector
	≥ 2 hits in different muon detector planes
	≥ 1 hit in the pixel detector
	≥ 6 hits in the tracker system
	Muons opposite in charge
	$80\,\mathrm{GeV} < M_{\mathrm{inv}}(\mu_1, \mu_2) < 100\,\mathrm{GeV}$
Candidate track selection	Good quality selection
	Kinematic selection
	Lepton/jet veto
	Isolation selection

Indeed, when testing this procedure in a $Z \to \ell\bar{\ell}$ + jets sample, it is found out, that a high purity can be achieved. This is illustrated in Fig. **??**, where the generator-level particle type which can be matched to the candidate track is shown. As can be seen, 95% of the selected tracks can not be matched to a generator-level particle.

When there is addiditonally the candidate track selection on top, than this track must be a fake track, as nothing can be further in the event.

It was also checked that the fake rate is constant for different processes . In figure bla, one can the the fake rate for the most important sm processes.

The zll events events are selected with the following requirements. blablabla

- Show plot with fake rate in different samples

- Show dependency of fakes for the number of hits
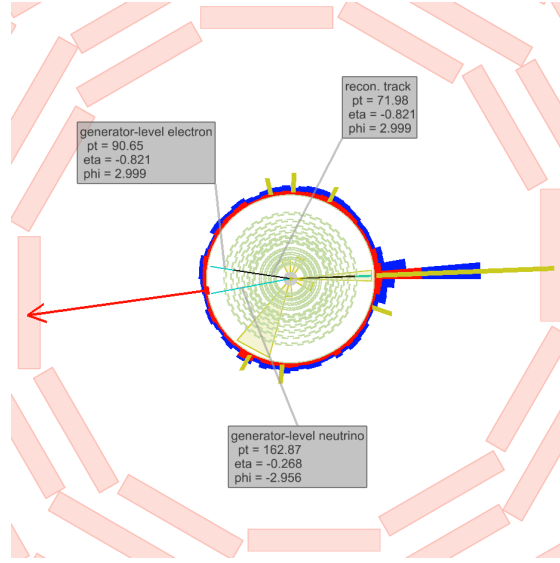
- Show ias plot for fakes

Figure 6.3: Visualisation of an $W \to e\nu_e$ event contributing to the SM background. In light blue the generator-level particles e and ν_e of the W decay are shown. The ν_e, only weakly interacting does not show any signature in the detector, whereas the electron ($p_T \simeq 90\,\text{GeV}$) leaves a track (black line) with $p_T \simeq 70\,\text{GeV}$ in the tracker. No ECAL energy deposits in the direction of the electron are visible. This is caused by the fact that the corresponding ECAL energy deposits were not read out in this event. An ISR jet ($p_T \simeq 230\,\text{GeV}$) causes the $\not{E}_T$ (read arrow) in the event.

- Explain background estimation method

6.2 Leptonic background

The leptonic background of the presented search is caused by non-reconstructed leptons which undergo hence the lepton veto selection. However, at least non-reconstructed electrons or taus should in principle deposit enough energy in the calorimeters such that they can still be vetoed by the calorimeter isolation requirement. As muons don't deposit much energy in the calorimeters, this reason does not hold for them. In the following, the sources of the three different leptonic backgrounds shall be characterised.

Electrons

To avoid the background source from unreconstructed electrons, all tracks pointing to a dead or noisy ECAL cells are vetoed, as described in the previous section. By this selection, almost all electrons are efficiently rejected. In the simulated $W + \text{jets}$ sample only one simulated event remains which pass all candidate track selection criteria and where the candidate track can be matched to a generator-level electron. This event is visualised in Fig 6.3. In this event no energy deposits in the ECAL are read out, which suggests, that this ECAL tower was neither working properly in 2012. Additionally, electrons can do
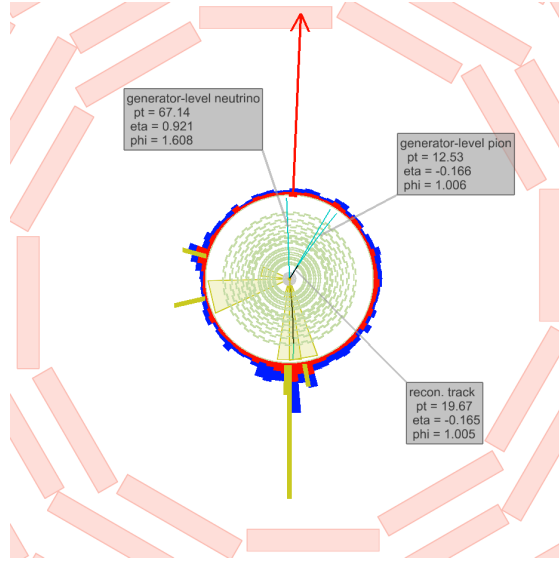
Figure 6.4: Visualisation of a $W^+ \to \tau^+ \nu_\tau \to \pi^+ \nu_\tau$ event contributing to the SM background. In light blue the generator-level particles π^+ and ν_τ are shown. The reconstructed track (black line) is very short because the pion interacts with the tracker material via the strong force.

bremsstrahlung which can change the direction of the electron significantly. Thus, the energy deposits in the ECAL can possibly not be matched to the original electron.

Taus

The tau background is contributing through the hadronic decay of a tau lepton to one charged pion $\tau \to \pi^\pm \nu$. Unreconstructed taus are typically low energetic and can therefore bypass the calorimeter isolation criterion. Because of nuclear interactions in the tracker, they can result in short reconstructed tracks which can easily be highly mismeasured in p_T. Thus, pions can also contribute even when imposing a tighter selection in the transverse momentum. Such an event is shown in Fig. 6.4.

Muons

Muons can fail reconstruction when they are pointing towards a bad cathode strip chamber. This is taken into account in the candidate track selection. However, some of the muons still fail reconstruction when they fall within the gap between stations 0 and 1 of the DT system at $\eta = 0.25$. The muon reconstruction efficiency drops from around 99% to a value of around 94% as shown in [29,30]. This possibility is illustrated in a simulated event shown in Fig 6.5. In [29,30] events are rejected when the track is pointing in a region of $0.15 < |\eta| < 0.35$. In this search, this cut was omitted to maximise signal acceptance. Due to the additional selection in I_{as}, muons can easily be efficiently suppressed. E.g. in the event example shown in Fig 6.5, the muon has an I_{as} value of about 0.02.
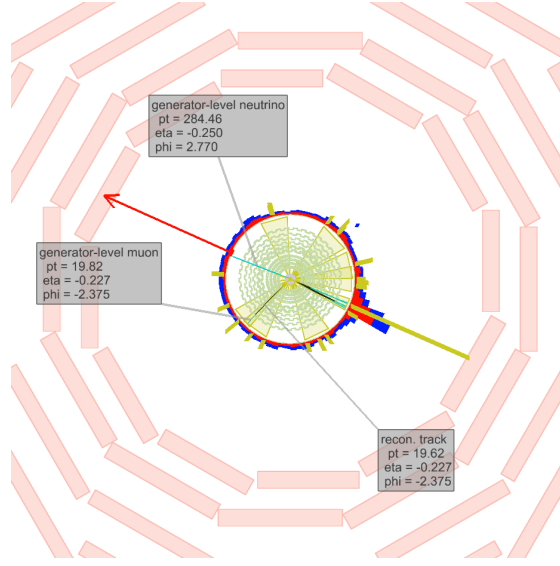
Figure 6.5: Visualisation of an $W \to \mu\nu_\mu$ event contributing to the SM background. In light blue the generator-level particles μ and ν_μ of the W decay are shown.
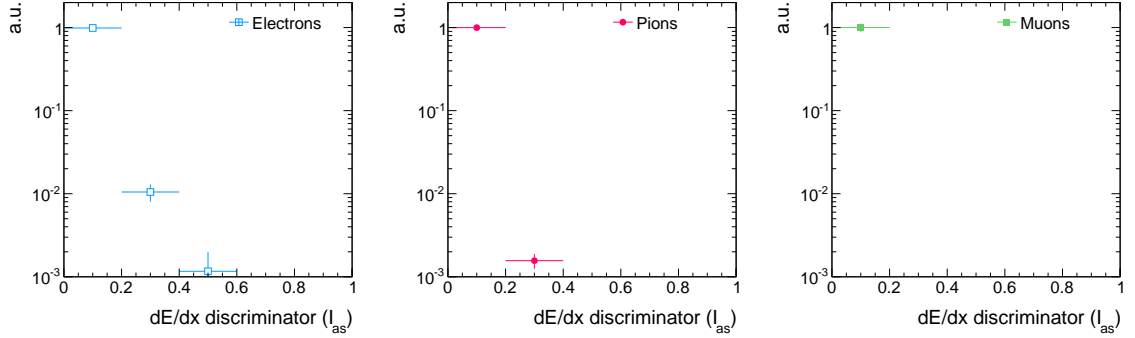

Figure 6.6: Normalised I_{as} distribution for electrons (left), pions (middle) and muons (right). For all leptons the I_{as} distribution is rapidly falling.

In general, all leptons are minimal ionising. However, as electrons are much lighter compared to muons or pions, they loose more energy also via radiative effects. Still, all three lepton types loose much less energy compared to hypothetical new heavy particles. To have the possibility to make an optimisation in the two main discriminating variables p_T and I_{as}, the background estimation methods are designed to work for all different p_T and I_{as} selection cuts. A comparison of the I_{as} distribution for all four different background sources is shown in Fig 6.6.

6.3 Systematic uncertainties

- Background consist of particles which make high energy deposits and are high pt

- In general: Low background search

7 Optimisation of search sensitivity

- Show plots

- show table

- Include NlostOuter here, too

8 Results

- Data cutflowtable

- Tables with results

- One plot (4 bins: Prediction and data)

9 Interpretation

9.1 Systematic uncertainties of simulated signal samples

9.2 Statistical Methods/ Limit setting

9.3 Exclusion limits

- 1-d limits

- 2-d limits

Bibliography

[1] CMS Collaboration, "Search for new physics in the multijet and missing transverse momentum final state in proton-proton collisions at $\sqrt{s}=$ 8 TeV", *JHEP* **06** (2014) 055, `arXiv:1402.4770`. `doi:10.1007/JHEP06(2014)055`.

[2] CMS Collaboration, "Searches for Supersymmetry using the M_{T2} Variable in Hadronic Events Produced in pp Collisions at 8 TeV", *JHEP* **05** (2015) 078, `arXiv:1502.04358`. `doi:10.1007/JHEP05(2015)078`.

[3] ATLAS Collaboration, "Search for squarks and gluinos with the ATLAS detector in final states with jets and missing transverse momentum using $\sqrt{s} = 8$ TeV proton–proton collision data", *JHEP* **09** (2014) 176, `arXiv:1405.7875`. `doi:10.1007/JHEP09(2014)176`.

[4] M. Ibe, S. Matsumoto, S. Shirai et al., "Wino Dark Matter in light of the AMS-02 2015 Data", *Phys. Rev.* **D91** (2015), no. 11, 111701, `arXiv:1504.05554`. `doi:10.1103/PhysRevD.91.111701`.

[5] T. Moroi, M. Nagai, and M. Takimoto, "Non-Thermal Production of Wino Dark Matter via the Decay of Long-Lived Particles", *JHEP* **07** (2013) 066, `arXiv:1303.0948`. `doi:10.1007/JHEP07(2013)066`.

[6] CMS Collaboration, "Searches for long-lived charged particles in pp collisions at $\sqrt{s}=$7 and 8 TeV", *JHEP* **07** (2013) 122, `arXiv:1305.0491`. `doi:10.1007/JHEP07(2013)122`.

[7] CMS Collaboration, "Search for disappearing tracks in proton-proton collisions at $\sqrt{s} = 8$ TeV", *JHEP* **01** (2015) 096, `arXiv:1411.6006`. `doi:10.1007/JHEP01(2015)096`.

[8] CMS Collaboration, "Reinterpreting the results of the search for long-lived charged particles in the pMSSM and other BSM scenarios", *CMS Physics Analysis Summary* **CMS-PAS-EXO-13-006** (2014).

[9] CMS Collaboration, "Search for disappearing tracks in proton-proton collisions at $\sqrt{s} = 8$ TeV", *Public CMS Wiki* (2015). https://twiki.cern.ch/twiki/bin/view/CMSPublic/PhysicsResultsEXO12034, Topic revision: r9.

[10] CMS Collaboration, "Phenomenological MSSM interpretation of the CMS 2011 5fb-1 results", *CMS Physics Analysis Summary* **CMS-PAS-SUS-12-030** (2013).

[11] CMS Collaboration, "Description and performance of track and primary-vertex reconstruction with the CMS tracker", *JINST* **9** (2014), no. 10, P10009, `arXiv:1405.6569`. `doi:10.1088/1748-0221/9/10/P10009`.

[12] H. Bethe, "Theory of the Passage of Fast Corpuscular Rays Through Matter", *Annalen Phys.* **5** (1930) 325–400. [Annalen Phys.397,325(1930)]. `doi:10.1002/andp.19303970303`.

[13] "National Institute of Standards and Technology". `http://physics.nist.gov/cgi-bin/Star/compos.pl?mode=text&matno=014`. Accessed: 2015-10-21.

[14] Particle Data Group Collaboration, "Review of Particle Physics", *Chin. Phys.* **C38** (2014) 090001. `doi:10.1088/1674-1137/38/9/090001`.

[15] L. Landau, "On the energy loss of fast particles by ionization", *J. Phys.(USSR)* **8** (1944) 201–205.

[16] H. Bichsel, "Straggling in Thin Silicon Detectors", *Rev. Mod. Phys.* **60** (1988) 663–699. `doi:10.1103/RevModPhys.60.663`.

[17] L. Quertenmont, "Search for Heavy Stable Charged Particles with the CMS detector at the LHC". PhD thesis, Louvain, U., 2010.

[18] T. W. Anderson, "On the Distribution of the Two-Sample Cramr-von Mises Criterion", *The Annals of Mathematical Statistics* **33** (1962), no. 3, pp. 1148–1159.

[19] F. James, "Statistical methods in experimental physics". 2006.

[20] CMS Collaboration, "Tracking and Vertexing Results from First Collisions", *CMS Physics Analysis Summary* **CMS-PAS-TRK-10-001** (2010).

[21] R. Gavin et al., "FEWZ 3.1: A User's Guide". `http://www.hep.anl.gov/fpetriello/FEWZManual_3.1.pdf`. Accessed: 2015-10-27.

[22] M. Czakon, P. Fiedler, and A. Mitov, "Total Top-Quark Pair-Production Cross Section at Hadron Colliders Through $O(\frac{4}{S})$", *Phys. Rev. Lett.* **110** (2013) 252004, `arXiv:1303.6254`. `doi:10.1103/PhysRevLett.110.252004`.

[23] J. Alwall, R. Frederix, S. Frixione et al., "The automated computation of tree-level and next-to-leading order differential cross sections, and their matching to parton shower simulations", *JHEP* **07** (2014) 079, `arXiv:1405.0301`. `doi:10.1007/JHEP07(2014)079`.

[24] T. Sjostrand, S. Mrenna, and P. Z. Skands, "PYTHIA 6.4 Physics and Manual", *JHEP* **05** (2006) 026, `arXiv:hep-ph/0603175`. `doi:10.1088/1126-6708/2006/05/026`.

[25] GEANT4 Collaboration, "GEANT4: A Simulation toolkit", *Nucl. Instrum. Meth.* **A506** (2003) 250–303. `doi:10.1016/S0168-9002(03)01368-8`.

[26] J. Allison et al., "Geant4 developments and applications", *IEEE Trans. Nucl. Sci.* **53** (2006) 270. `doi:10.1109/TNS.2006.869826`.

[27] B. Fuks, M. Klasen, D. R. Lamprea et al., "Gaugino production in proton-proton collisions at a center-of-mass energy of 8 TeV", *JHEP* **1210** (2012) 081, `arXiv:1207.2159`. `doi:10.1007/JHEP10(2012)081`.

[28] B. Fuks, M. Klasen, D. R. Lamprea et al., "Precision predictions for electroweak superpartner production at hadron colliders with Resummino", *Eur.Phys.J.* **C73** (2013) 2480, `arXiv:1304.0790`. `doi:10.1140/epjc/s10052-013-2480-0`.

[29] J. D. Brinson, "A search for disappearing tracks in proton-proton collisions at $\sqrt{s} = 8$ TeV". PhD thesis, Ohio State U.

[30] C. H. J. Brinson and W. Wulsin, "Search for disappearing tracks", *CMS Analysis Note* **CMS-AN-12-400** (2014). Internal documentation.

[31] CMS Collaboration, "Tracking and Primary Vertex Results in First 7 TeV Collisions", *CMS Physics Analysis Summary* **CMS-PAS-TRK-10-005** (2010).

[32] A. B. et. al., "Search for New Physics in the Monojet final state at CMS", *CMS Analysis Note* **CMS-AN-12-421** (2012). Internal documentation.

[33] CMS Collaboration, "Search for dark matter, extra dimensions, and unparticles in monojet events in protonproton collisions at $\sqrt{s} = 8$ TeV", *Eur. Phys. J.* **C75** (2015), no. 5, 235, `arXiv:1408.3583`. `doi:10.1140/epjc/s10052-015-3451-4`.